DEVELOPMENT OF LOW TEMPERATURE GAS SENSING FOR DETECTION OF VOLATILE ORGANIC COMPOUNDS AND METHANE DERIVED FROM CeO_2-TiO_2 HETEROSTRUCTURE

Submitted by

LANNETH MABUNDA [redacted]

In partial-fulfilment of the requirements for the degree

(MSc)

Master of Science

In

Physics

In the

FACULTY OF SCIENCE AND AGRICULTURE

(School of Physical and Mineral Sciences)

At the

University of Limpopo

Supervisor: Prof David E. Motaung

Co-supervisor: Dr Steven S. Nkosi

DECLARATION

I declare that the work hereby submitted by me to the University of Limpopo for the Master's degree in Physics, is my own work under the topic of **Development of Low Temperature Gas Sensing for Detection Of VOCs And CH_4 Derived From CeO_2-TiO_2 Heterostructure** and that all the sources that I have used or quoted have been indicated and acknowledged by means of complete references and that this work has not been submitted before for any other degree at any other institution.

Full names

LANNETH MABUNDA

....

Date

15/11/2022

....

Student number

[redacted]

....

Signature

……………………………….

ACKNOWLEDGEMENT

With enormous gratitude, I would like to thank my family for their support throughout my studies. Special thanks to supervisor, Prof David E. Motaung, and co-supervisor, Dr. Steven S. Nkosi, for their time and efforts they contributed towards my research project. I would also like to thank the Council for Scientific and Industrial Research (CSIR) for helping me financially, and finally, I would like to thank the University of Limpopo and the Department of physics for offering me the opportunity to enrol for the master’s program. The University of the Free State is also acknowledged for the instrumentations support.

ABSTRACT

Methane (CH_4) is a foremost hazardous gas in coal mines because of its explosive behavior. At concentrations of 30 000 to 50 000 ppm, CH_4 can result in an explosion. Though the current commercial obtainable noble metal/Al_2O_3 beads-based CH_4 sensors show higher selectivity and sensitivity toward CH_4 nonetheless, their operational temperature is extreme, i.e., 500−700 °C. Thus, at that temperature, the CH_4 combustion on the catalysts generally leads to a high risk of explosion and complexity in fabricating the sensor. Therefore, is very vital to develop CH_4 sensors that can function at lower temperatures. It is in the current study, the CeO_2, TiO_2, and TiO_2-CeO_2 heterostructures were prepared using the sol-gel method. The XRD analyses disclosed the formation of pure CeO_2, TiO_2, and TiO_2-CeO_2 heterostructure. While the surface analyses showed that nanostructures are made of nanoparticles. Moreover, the optical studies showed that the band of the pure CeO_2, TiO_2, and TiO_2-CeO_2 heterostructures is dependent on the synthesis temperature. The bandgap reduced when increasing the synthesis temperature for all the nanostructures. However, in terms of gas sensing, more especially for the detection of CH_4, the CeO_2, TiO_2, and TiO_2-CeO_2 heterostructure-based sensors showed no sensing response at low operational temperatures, instead, the sensors could only function beyond 300 °C, which was higher than the limit of our sensing station.

In chapter 5, the n-n type of TiO_2/CeO_2, CeO_2/TiO_2, p-n-n type of Cr_2O_3/TiO_2/CeO_2 and p-n-n type of Cr_2O_3/CeO_2TiO_2-ternary heterostructures were pared using hydrothermal method. Structural analyses validated the formation of prepared heterostructures. While scanning electron microscopy showed that the nanostructures are made of nanoparticles. For gas sensing application, the sensors

were tested toward various gases, including benzene, ethylbenzene, toluene (BTE), ethanol, carbon monoxide, methane (CH_4), carbon dioxide (CO_2), and nitrogen dioxide (NO_2). Among the tested sensors, the $Cr_2O_3/TiO_2/CeO_2$-based sensor displayed a remarkable response and selectivity toward CH_4 at a low operational temperature of 100 °C. The higher response observed for the $Cr_2O_3/TiO_2/CeO_2$-based sensor towards CH_4 was further validated by photoluminescence (PL) studies, which showed that the material consisted of higher oxygen vacancies (V_O) which could be the reason for improved sensing performance. Additionally, the UV-vis analyses also confirmed that the material has a smaller bandgap, which denoted that the electrons were more inclined to change and resulting in more photogenerated carriers that could lead to enhanced sensing response and therefore lead to reduced sensing temperature. Therefore, these results denote that the $Cr_2O_3/TiO_2/CeO_2$-based sensor could be considered as the potential candidate for the detection of CH_4 at low temperatures.

TABLE OF CONTENT

LIST OF FIGURES

LIST OF TABLES

CHAPTER 1

1. Introduction

1.1 Background of Gas Sensors

In the 19th and 20th Centuries, coal miners wanted to find out if the mine contained methane gas (CH_4) at the working arears, i.e., underground. As a result, several mine workers had to wear flame lights on their helmets to see and detect the tremendously combustible methane.

The initial approach for CH_4 was based on allowing one miner, who is shielded in a wet blanket and holding a long wick with a flame on the end. The miner was advised to run the taper along the mine walls searching for CH_4 pockets, which may be released and sometimes ignite without creating any harm to the miner, though at times it could ignite the entire area and leads kill the miner. The idea by then was based on losing one miner than the entire team. Then, this gas detection evolved from using humans to canaries, which helped by reducing the loss of lives and offering a visible and distinct gas detection approach.

Then later, the next evolution was based on flame safety light **(see Fig. 1.1(a))**, which was more useful in illuminating the mines and offering better precision for CH_4 detection. This then moved to the catalytic sensor (**see Fig. 1.1(b))**, which was the first gas sensing detector, which resembled current technology. The catalytic sensor operation is based on detection the of temperature variation that is relative to the concentration of gas **[1.1]**.

Nonetheless, the current chemical gas sensor (**see Fig. 1.1(b))** technology is based on detecting the analyte target gas at various concentrations, as a result the corresponding change in resistance will be observed. This typedof a sensor is used to detect gas leaks and other emissions. In other words, gas detectors can be used to detect various toxic, flammable, and hazardous gases **[1.1-1.5]**.

Fig. 1.1: Images showing (a) flame safety light, (b) catalytic sensor and (c) chemiresistive sensor **[1.1.-1.3]**.

1.2. Gas Sensors Classification

Gas sensor comprises of an active layer, substrate, electrode, and heater. A schematic is shown in **Fig. 1.2**. **Fig. 1.2(b)** shows a clear overview of the electrode, and heater. The sensitive layer is deposited on the substrate and interacts with the target gas. Changes caused by the presence of the analyte are measured by the electrode and displayed as an analytical signal that can be interpreted. The heater regulates the working temperature of the sensor. The material used as sensitive layer determines the working principle and type of gas sensor and the sensor performance is measured in terms of change in chemical or physical property of the sensitive layer. Currently, several sensors exist as depicted in **Fig. 1.3(a)** and they discussed briefly in the section below.

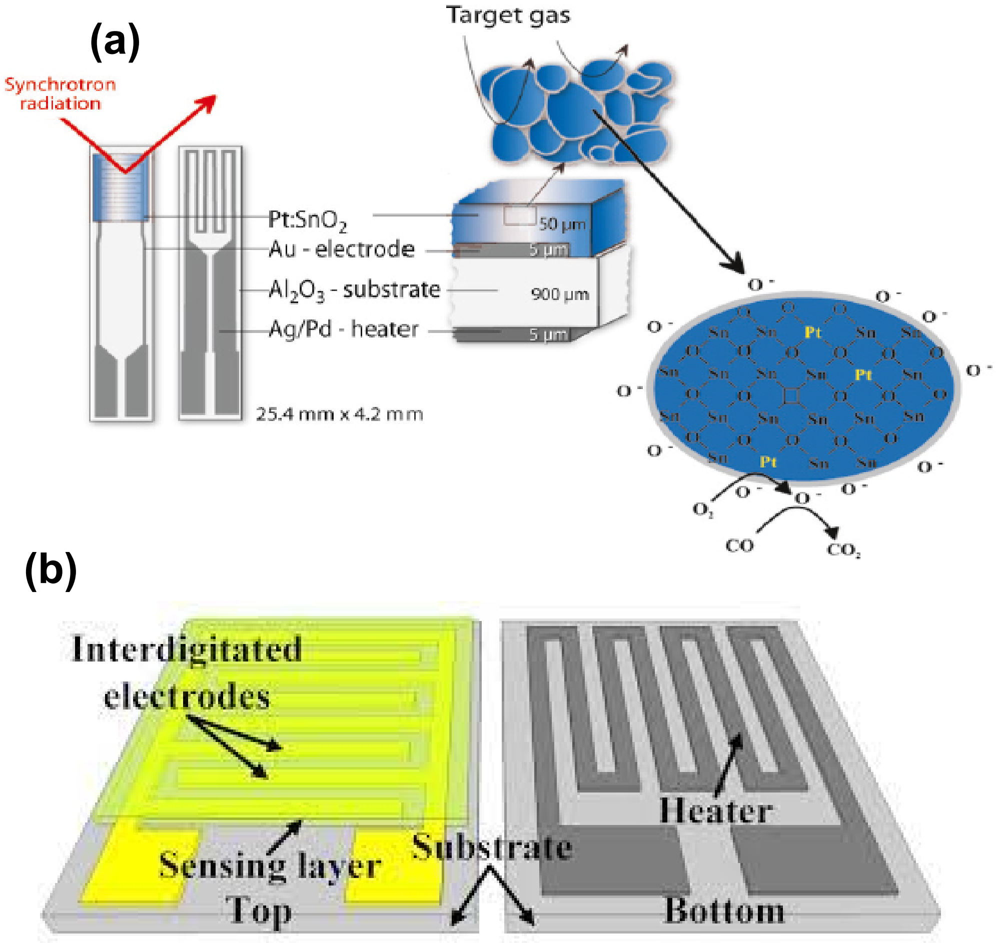

Fig. 1.2: (a) Diagram interpretation of the sensor device. Schematic drawing showing the influence of Pt additives in the CO gas sensing with SMO SnO_2-based gas sensor, (b) shows the clear overview of the electrodes and heater lying at the top and bottom of the substrate **[1.6].**

1.2.1. Chemical gas sensors

In 1991, International Union of Pure and Applied Chemistry (IUPAC) defined the so-called chemical sensors. This kind of a sensor converts chemical information, which ranges from concentration of an explicit sample constituent to total composition analysis, into a systematically valuable signal **[1.7]**.

1.2.2. Optical gas sensors

The optical based gas sensors detect the change in physical characteristics, like intensity, colour, emission spectra, polarization, etc. that are induced by absorbance, fluorescence, reflectance, or light scattering of a specific wavelength by the gas **[1.8]**.

1.2.3. Electrochemical gas sensors

This typical gas sensor entails of electrochemical cells, which are completed from two electrodes, (1) sensing electrode and, (2) reference electrode, which are coupled over a thin electrolyte layer. This sensor permits the gas diffusion via a membrane to the sensing electrode, which is where the gas oxidation/reduction occur **[1.8]**.

1.2.4. Catalytic gas sensor

Generally, most of the semiconductor metal oxides have catalytic features. Flammable gas mixtures are generally not burning till they attain a particular or threshold ignition temperature. However, the combustion of the gas will start even at lesser temperatures in the existence of a detailed chemical process. This process is recognized as catalytic combustion. Thus, the sensor created on catalytic principle is defined as a catalytic gas sensor **[1.8]**.

1.2.5. Mass sensitive gas sensor

In thin kind of sensor, the target analyte gas is mounted on the sensitive layer due to the mass of the sensor surface variations. The examples of mass sensitive sensors are surface acoustic wave and quartz crystal microbalance-based sensors. The change in mass displays the variation in the characteristics associated with the sensitive material **[1.9]**.

1.2.6. Magnetic gas sensors

The change in the paramagnetic properties of the analyte is the basic principle of magnetic sensors [55]. These sensors are represented by a certain type of oxygen monitor because oxygen has a high magnetic susceptibility as compared to other gases [56]. Therefore, a gas sensor based on the paramagnetic principle and Pauli's exclusion principle for oxygen can be built with only minor cross sensitivities.

1.2.7. Thermometric gas sensors

In typical sensors, chemical reactions occur once the sensor layer interacted with the gases. As a result, these chemical reactions are the reason for the change in temperature. Basically, these changes are denoted by the variation in resistance, current and voltage. Since the sensor has a temperature probe, which is coated with a chemically selective layer. Therefore, the sensor functions by sensing the transfer of heat when the sensor interacts with the analyte gas **[1.8]**.

1.2.8. Photoacoustic spectroscopy

Today, gas phase spectroscopy has become popular in several fields, such as medical sciences, chemistry, etc. This gas sensor is spectroscopy is constructed on the photoacoustic effect **[1.10]**. The spectroscopic gas sensors have proved to be invaluable tools. Various ways of utilizing these gas sensors exist. For this sensor, it is not necessary for sample preparation and maintenance **[1.11]**.

1.2.9. Chemiluminescence

This is one of the luminescent phenomena, which may be defined as the emission (Ultra-Violet, Visible or Infra-Red) produced by a chemical reaction. The detection of this sensor is well-known for higher sensitivity, rapid response, and nonappearance of undesirable luminescence in the background **[1.12]**.

1.2.10. Gas chromatography

Gas chromatography (GC) is extensively utilized for the purpose of quality control and extra detection and to quantify the components in a combination. This technique is mostly utilized as a device to identify very small quantities of possible components or constituents. Further details around this technique can be found in ref. **[1.13]**.

1.2.11. Metal oxide semiconductor-based gas sensors

In the previous years, various kinds of gas sensors were fabricated, more especially for detection of flammable gases, such as CH_4, etc., as discussed in section 1.1. **[1.14]**. Among the previously fabricated sensors, semiconductor metal oxide (SMO) MOS-based gas sensors have attracted a significant interest because of their low-cost, easy-fabrication, higher sensitivity and low limit of detection **[1.15]**. Moreover, SMO-based sensors have been very useful for detection of different dangerous gases, like CO_2, SO_2, CH_4, LPG, CO, etc. Generally, among the used SMO materials, SnO_2, ZnO and WO_3 are the most used materials for gas sensing, as depicted in **Fig. 1.3(b)**. Several synthesis approaches exit for the preparation of SMOs, which include, hydrothermal, sol-gel method, chemical vapour deposition, co-precipitation, sputtering, thermal evaporation, etc. **[1.16, 1.17]**. Currently, two main kinds of SMO based sensors exists, which include n-type and p-type SMO. For the n-type, the greater part charge carriers are electrons and p-type, the majority charger carriers are holes **[1.18]**. The mechanisms associated with gas sensing, like gas reaction, rate of reaction and gas selectivity are strongly influenced due to the porosity, surface of the material, introduction of catalysts and the operational temperature **[1.19]**.

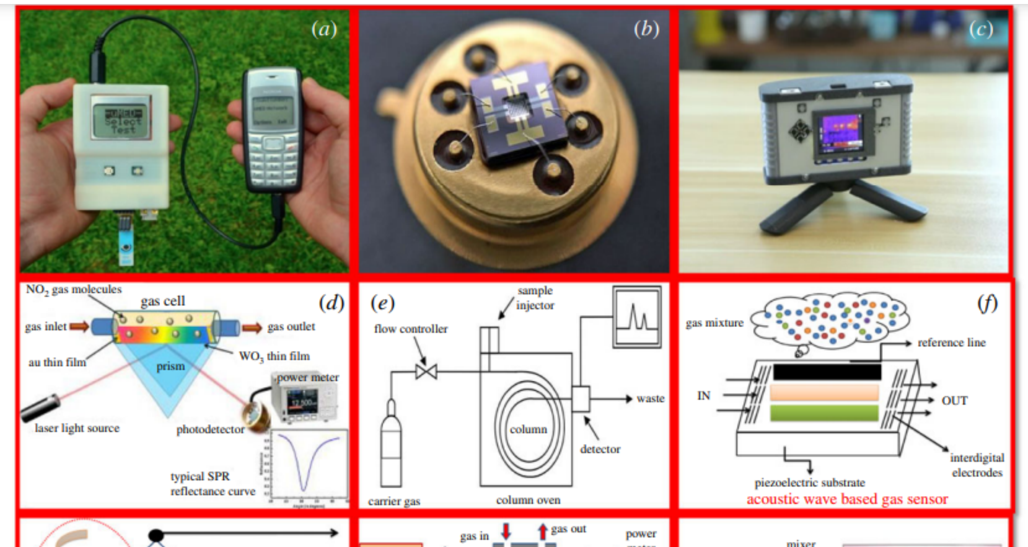

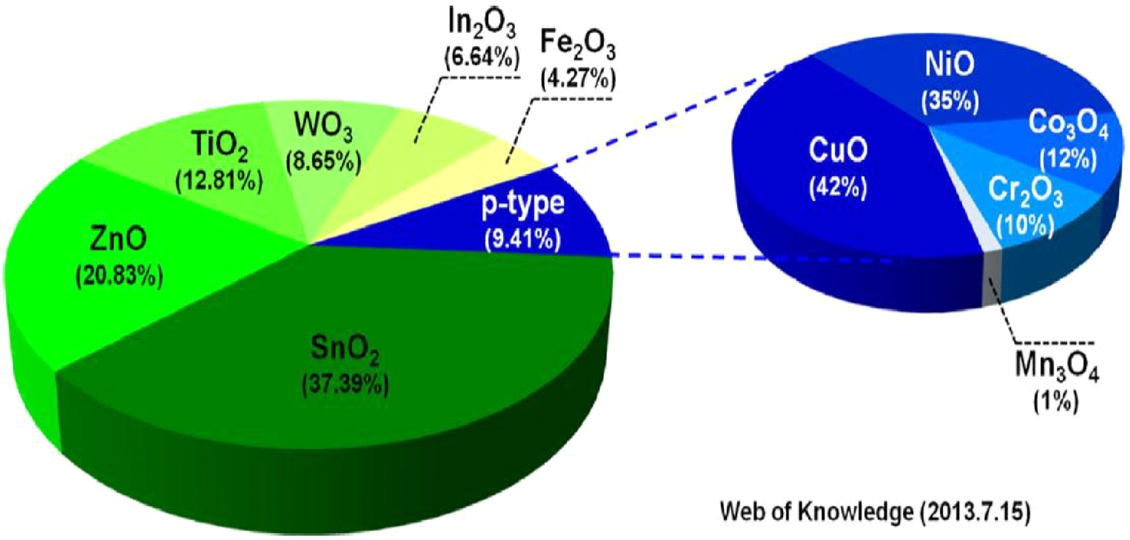

Fig. 1.3. (a) Electrochemical sensor in the arrangement of a device [1.19], (b) SMO-based sensor [1.20], (c) thermal sensor, in the arrangement of camera [1.21], (d) optical sensor [1.22], (e) gas chromatography, (f) mass sensitive sensor, (g) catalytic-based sensor, (h) photoacoustic spectroscopy, (i) chemiluminescence, (j) magnetic-based sensor, and (k) chemical-based sensor.

1.3 Global Demand for Sensors

In 2019, the worldwide gas sensor market was valued at $2,19dbillion and is anticipated to grow at 8.3% CAGR between 2020 and 2027. Gasdsensorsdare used to measure the concentration of various nearby gases, such as oxygen,dcarbon dioxide,dnitrogen oxides.dThese sensors are outfitted with very sensitive sensing components that are powered by circuit-connected wires. These sensors are widely used in the manufacturing and processing industriesdtoddetect various toxic substances such as hydrogendsulfide and nitrogenddioxide **[1.23, 1.24]**.

Statistics below show the size of the US end-use market (in millions of dollars) from 2016 to 2027.

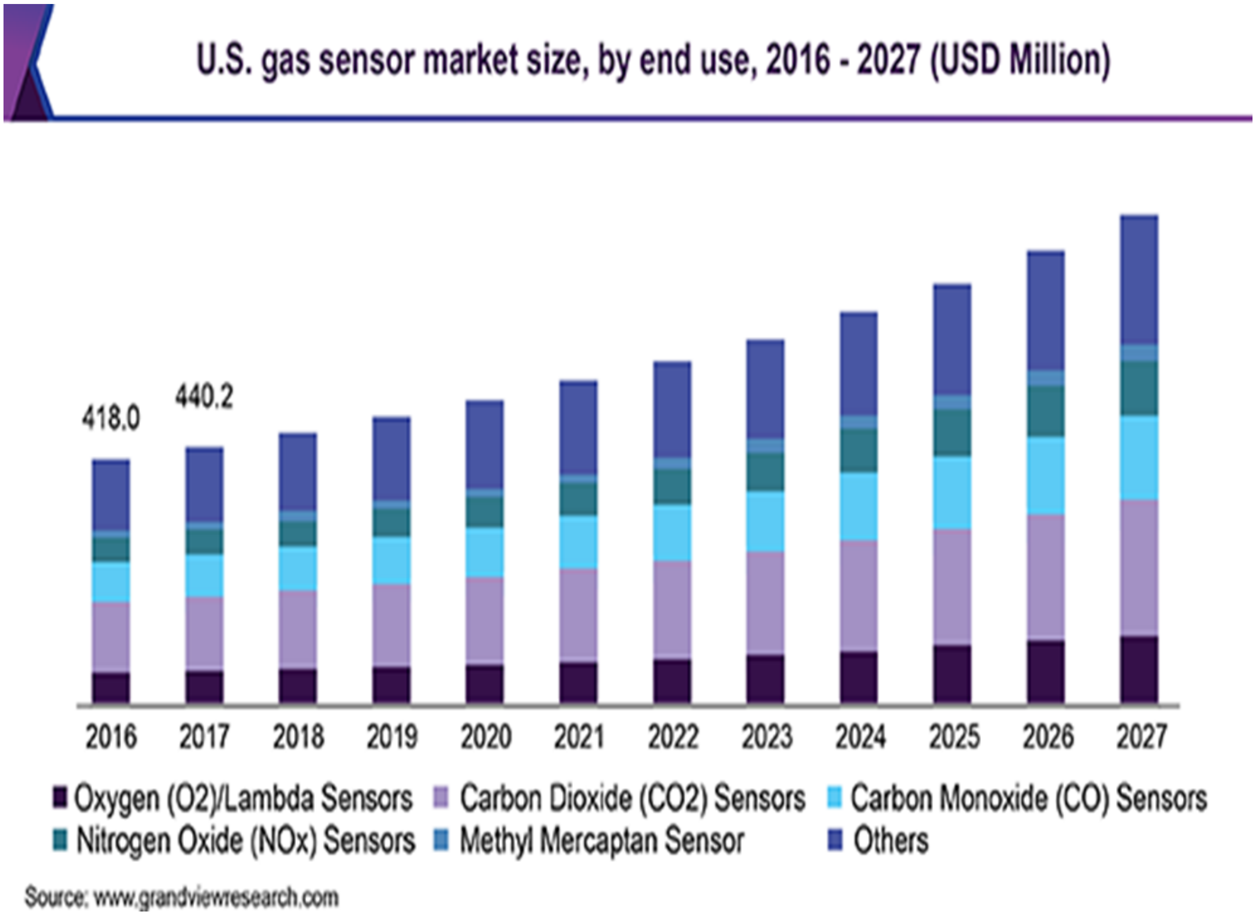

Source: www.grandviewresearch.com

Fig.1.4: Schematic diagram of the US gas sensor market **[1.25].**

1.4 Problem Statement

This project is motivated by apprehensions of several deaths occurring yearly in several industries, such as mining sectors, workplaces, etc. due to exposure of methane gas. Currently, due to its necessity to be used as source of energy for domestic and industrial applications **[1.26]**, at higher concentration CH_4 can cause asphyxiation by reducing the percentage of O_2 in a sealed room and further resulting in sick building syndrome having symptoms like headache, irritation of the throat irritation, scratchy skin, faintness, and fatigue in human being **[1.26]**. This may explain the reason why the patient loses consciousness **[1.27]**. At concentrations higher than 30 000-40 000 ppm, CH_4 can create explosion, more especially in workplaces, such as mining environment. Though the current commercial obtainable noble metal/Al_2O_3 beads-based CH_4 sensors show higher selectivity and sensitivity toward CH_4 nonetheless, their operational temperature is extremely, i.e., 500−700 °C. Thus, at that temperature, the CH_4 combustion on the catalysts generally leads in a high risk of explosion and complexity in fabricating the sensor **[1.28, 1.29]**. Besides, the higher operational temperature can also lead to unwanted long-term drift issues because of sintering properties in the grain boundaries **[1.30, 1.31]**. Therefore, the focus of the current study is to improve the stability and sensitivity of the metal oxide based sensors towards CH_4 by operating at low temperature as to reduce the sintering problems in grain boundaries. As a result, the current project attempts to use metal oxide CeO_2-TiO_2 heterostructure by introducing the p-type Cr_2O_3 on the surface of either CeO_2/TiO_2 or TiO_2/CeO_2 heterostructure to form a ternary structure as a gas sensing layer for the detection of CH_4 gas.

1.5 Aim:

The aim of the study is to develop a low operating temperature gas sensor for detection of CH_4 gas using a CeO_2 -TiO_2 heterostructure.

1.6 Objectives

The objectives of the study are to:

I. synthesize the pure CeO_2, TiO_2 and CeO_2 – TiO_2 and Cr_2O_3/CeO_2/TiO_2 Cr_2O_3/ TiO_2/CeO_2 heterostructures using the sol-gel and hydrothermal method.

II. study the structure, point defects, paramagnetic properties of the materials

III. study the active surface of the individual and CeO_2 – TiO_2 and Cr_2O_3/ CeO_2 – TiO_2 heterostructures

IV. fabricate and test the sensing materials for their sensitivity and selectivity in CH_4 detection in the existence of several interference gases (Sulphur dioxide, carbon monoxide, hydrogen, hydrogen sulfide, benzene, toluene, xylene, propanol, nitrogen dioxide, etc.)

V. study the sensor response mechanism on CeO_2 – TiO_2 and Cr_2O_3/ CeO_2 – TiO_2 films in a wide temperature range.

VI. design, optimize and fabricate of CeO_2 – TiO_2 and Cr_2O_3/ CeO_2 – TiO_2 gas sensors.

VII. investigate the long-term stability of the sensor material for more than 6 months in the presence of relative humidity.

1.6 Thesis Outline

Chapter one focuses on the background of gas sensors, types and classification of gas sensors, gas sensor market and problem statement.

Chapter two deals with the literature around the properties of TiO_2, CeO_2, and $Cr2O_3$, and semiconductor metal oxides gas sensors associated with TiO_2, CeO_2, and $Cr2O_3$ for methane detection.

Chapter three focuses on the characterization techniques used to characterize the used materials in this work.

Chapter four focuses on the structure, and optical properties of CeO_2, TiO_2, and TiO_2-CeO_2 nanostructures prepared using sol-gel method.

Chapter five deals with the different synthesis approach of $Cr_2O_3/TiO_2/CeO_2$ ternary heterojunction-based sensor for improved CH_4 performance.

Chapter six provides the summary/conclusion and future work.

1.8 References

[1.1] https://www.esrf.fr/UsersAndScience/Publications/Highlights/2011/dynamics/dyn7

[1.2] https://dsasuppliers.com/blog/a-brief-history-of-gas-detection/

[1.3] https://royalsocietypublishing.org/doi/10.1098/rsos.201324 (2020, October 19). Gas detector. In *Wikipedia, The Free Encyclopedia*. Retrieved 11:06, November3,2020,from https://en.wikipedia.org/w/index.php?title=Gas_detector&oldid=984312199

[1.4] Z.P. Tshabalala, T.P Mokoena, M. Jozela, J. Tshilongo, T.K Hillie, H.C Swart, D.E Motaung, TiO_2 Nanowires for Humidity-Stable Gas Sensors for Toluene and Xylene ACS Applied Nano Materials, 4 (2021) 702-716.

[1.5] MS Mamabolo, ZP Tshabalala, HC Swart, GE Mphaphuli, TK Hillie, DE Motaung, Low Temperature Tunability on CO Selectivity, Low Detection Limit Based on SnO2-Hollowspheres Induced by Various Bases, Surfaces and Interfaces 31 (2022) 101954.

[1.6] https://pure.tudelft.nl/ws/portalfiles/portal/71472283/Sokolovskij_GaN_sens_dissertation_V2.pdf.

[1.7] Bi H, Han X. 2019 Chemical sensors for environmental pollutant determination. In Chemical, gas, and biosensors for internet of things and related applications, pp. 147–160. Amsterdam, The Netherlands: Elsevier.

[1.8] Fraden J. 2010 Handbook of modern sensors. New York: NY: Springer.

[1.19] Gautam YK, Sharma K, Tyagi S, Ambedkar AK, Chaudhary M, Pal Singh B. 2021 Nanostructured metal oxide semiconductor-based sensors for greenhouse gas detection: progress and challenges. R. Soc. Open Sci. 8: 201324. https://doi.org/10.1098/rsos.201324

[1.10] Bell AG. 1880 On the production and reproduction of sound by light. Am. J. Sci. s3-20, 305–324. (doi:10.2475/ajs.s3-20.118.305)

[1.11] Harren FJM, Cristescu SM. 2019 Photoacoustic spectroscopy in trace gas monitoring. In Encyclopedia of analytical chemistry: applications, theory and instrumentation, pp. 1–29. Hoboken, NJ: John Wiley & Sons.

[1.12] Zhang L, Hu J, Lv Y, Hou X. 2010 Recent progress in chemiluminescence for gas analysis. Appl. Spectrosc. Rev. 45, 474–489. (doi:10.1080/ 05704928.2010.503527)

[1.13] Pravallika S. 2016 Gas chromatography: a mini review. Res. Rev. J. Pharm. Anal. 5, 2340–2347. 61. Arshak K, Moore E, Lyons GM, Harris J, Clifford S. 2004 A review of gas sensors employed in electronic nose applications. Sens. Rev. 24, 181–198. (doi:10.1108/02602280410525977).

[1.14] Arshak K, Moore E, Lyons GM, Harris J, Clifford S. 2004 A review of gas sensors employed in electronic nose applications. Sens. Rev. 24, 181–198. (doi:10.1108/02602280410525977)

[1.15] Manorama SV, Izu N, Shin W, Matsubara I, Murayama N. 2003 On the platinum sensitization of nanosized cerium dioxide oxygen sensors. Sens. Actuators B Chem. 89, 299–304. (doi:10.1016/S0925-4005(03)00005-4)

[1.16] Pearton SJ, Ren F, Wang YL, Chu BH, Chen KH, Chang CY, Lim W, Lin J, Norton DP. 2010 Recent advances in wide bandgap semiconductor biological and gas sensors. Prog. Mater. Sci. 55, 1–59. (doi:10.1016/j.pmatsci.2009.08.003)

[1.17] Kolmakov A, Moskovits M. 2004 Chemical sensing and catalysis by one-dimensional

[1.18] Pearce TC, Schiffman SS, Nagle HT, Gardner JW. 2003 Handbook of machine olfaction: electronic nose technology. Hoboken, NJ: Wiley-VCH Verlag GmbH & Co. KGaA, Weinheim.

[1.19] Choi JK, Hwang IS, Kim SJ, Park JS, Park SS, Jeong U, Kang YC, Lee JH. 2010 Design of selective gas sensors using electrospun Pd-doped SnO2 hollow nanofibers. Sens. Actuators B Chem. 150, 191–199. (doi:10.1016/j.snb.2010.07.013)

[1.20] Chaikarn L, Sukon AP. 2007 Effects of palladium loading on the response of thick film flamemade ZnO gas sensor for detection of ethanol vapor. Sensors 7, 1159–1182.

[1.21] Schaller E, Bosset JO, Escher F. 1998 'Electronic noses' and their application to food. LWT - Food Sci. Technol. 31, 305–316. (doi:10.1006/fstl. 1998.0376)

[1.22] Paliwal A, Sharma A, Tomar M, Gupta V. 2015 Room temperature detection of NO2 gas using optical sensor based on surface Plasmon resonance technique. Sensors Acutators B: Chemical 216, 497–503.

[1.23] Liu, X., Cheng, S., Liu, H., Hu, S., Zhang, D. and Ning, H., 2012. A survey on gas sensing technology. *Sensors*, *12*(7), pp.9635-9665.

[1.24] https://www.marketsandmarkets.com/Market-Reports/gas-sensor-market-245141093.htm.

[1.25] V. E. Bochenkov and G. B. Sergeev, , Chapter 2, Vol 3, American Scientific Publishers, (2010), pages 31-52.

[1.26] G.Y. Chai, O. Lupan, E.V. Rusu, G.I. Stratan, V.V. Ursaki, V. Şontea, H. Khallaf, L. Chow, Functionalized individual ZnO microwire for natural gas detection, Sensor Actuators A 176 (2012) 64–71

[1.27] K.C. Lam, B.L. Huang, S.Q. Shi, Room-temperature methane gas sensing properties based on in situ reduced graphene oxide incorporated with tin dioxide, J. Mater. Chem. 5 (22) (2017) 11131-11142.

[1.28] F. Liu, Y. Zhang, Y. Yu, J. Xu, J. Sun, G. Lu, Enhanced sensing performance of catalytic combustion methane sensor by using Pd nanorod/γ-Al2O3, Sens. Actuators B Chem. 160 (2011) 1091–1097.

[1.29] Jing Wang, Chenyu Hu, Yi Xi, Bo Zhang, Mesoporous ZnO nanosheets with rich surface oxygen vacancies for UV-activated methane gas sensing at room temperature, Sensors and Actuators: B. Chemical 333 (2021) 129547.

[1.30] D.E Motaung, Z.P Tshabalala, P.R Makgwane, F.A Mahmoud, D.N Oosthuizen, F.R Cummings, N. Leshabane, N. Hintsho-Mbita, X. Li, S. S Ray, H.C Swart, Multi-functioning of CeO2-SnO2 heterostructure as room temperature ferromagnetism and chemiresistive sensors, Journal of Alloys and Compounds, 906 (2022) 164317.

[1.31] E. Espid, F. Taghipour, Development of highly sensitive ZnO/In_2O_3 composite gas sensor activated by UV-LED, Sens. Actuators B 241 (2017) 828–839

CHAPTER 2

2.1.1 Structural properties

Cerium oxide (CeO_2) is an important material for various technological applications in sensors, solid electrolyte fuel cell technology, supercapacitors, oxygen sensors, oxygen membrane systems, polishing materials glass, thin film electronic materials and biotechnology.dIn addition to mixed electronic and ionic conductivity, high oxygen storage, and the ability to absorb and dissolve oxygen by conversion between Ce^{+3} and Ce^{+4}, high ionic conductivity (i.e the lack and mobility of oxygen vacancies), a chemical and medical environment due to a unique property **[2.1 - 2.2]**.

Cubic Cerium oxide (CeO_2) has a structure similar to fluorite. As one of the four most common rare earths, it has been selected as one of the rare earths by many researchers and is considered an important gate oxide material due to its unique properties. Properties: medium band gap (3.0-3.6 eV), high dielectric constant (k: 23-26), high refractive index (n:d2.2-2.8), high dielectric strength (~2.6 MV cm^{-1}) microelectrons. Cerium can exist in trivalent (Ce^{+3}) and tetravalent (Ce^{+4}) forms **[2.3-2.5]**. Cerium is oxidized in the space ring Fm3m, with Ce^{4+} in 8 coordinates and O^{2-} in 4 coordinates. At high temperatures, it releases oxygen and forms non-stoichiometric forms that lack the anions that support the fluorite lattice. The chemical formula of this material is $CeO_{(2-x)}$, where $0 < x < 0.28$. The value of x depends on the temperature, as well as the fracture zone and the partial pressure of oxygen **[2.6-2.7]**.

Cerium oxide (CeO_2) crystallizes in a lattice of mixed atoms of cerium and oxygen and zinc, occupying one of the two sublattices in the center of the cubic plane that forms this structure. This, 8, or cubic, 4, cylinder. The structure of a cerium-oxygen-zinc alloy with two interpenetrating fcc lattices of Ce and O. The lattice constant of the CeO_2 structure is 5.41 Å **[2.8-2.10]**.

Covalent bonds between the four neighbors in the tetrahedral structure, where the Ce atoms are located in the centered cubic lattice and the O atoms occupy places in the tetrahedral lattice. The CeO_2 unit cell is the basic unit, and the structure of the zinc alloy is close to diamond crystals, consisting of two interpenetrating cubic Bravais lattices. a = 5.41, b = 5.41 Å, c = 5.41 Å α = 90°, β = 90°, γ = 90° . The atomic positions of cerium (0,0,0) and oxygen (1/4,1/4,3/4) are 163.44 Å **[2.9-2.16]**. Check figure 2.1 below:

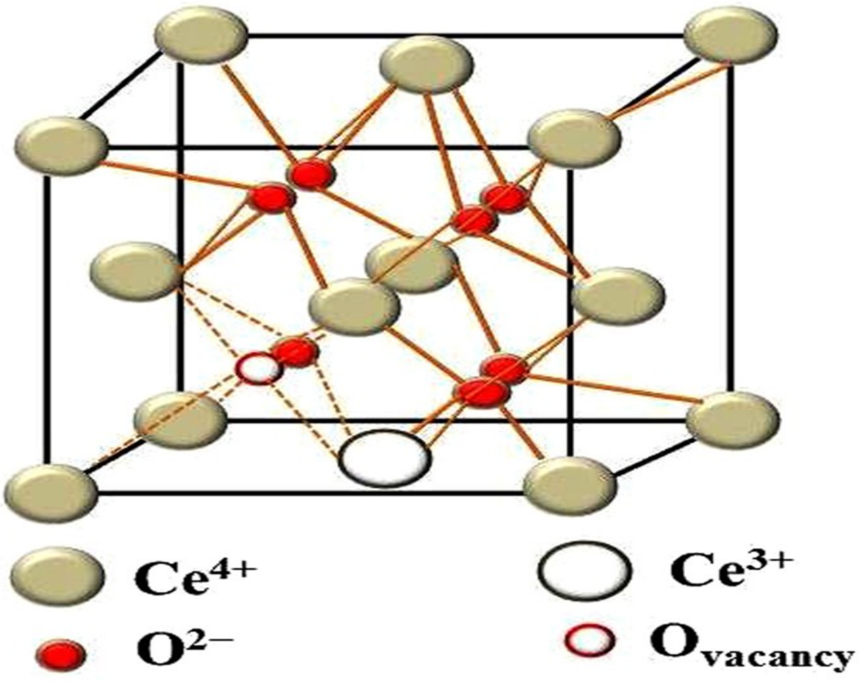

Fig. 2.1: Schematic diagram Cerium oxide (CeO_2) **[2.17].**

2.1.2 Electrical and Optical properties of Cerium Oxide (CeO_2)

Cerium Oxide (CeO_2) has a wide range of applications in various fields. Studies have shown that cerium oxide has excellent oxygen storage capacity due to its ability to reversibly react with oxygen to form Ce_2O_3. **[2.18]** Optical studies have shown that cerium oxide has the ability to block radiation in the UV range **[2.18-2.19]**. Its catalytic properties as a redox have been well studied and have played an important role in recent catalytic developments in the automotive industry **[2.20-2.22]**.

CeO_2 has exceptional optical properties, such as a high refractive index, good transmission in the visible and infrared and a wide band gap of 3.2 eV **[2.23]**. It is an attractive material due to its potential application as a passive counter electrode in smart electronic windows. CeO_2 exhibits +3 and +4 oxidation states suitable for valence change processes **[2.24-2.25]**. CeO_2 is an n-type semiconductor that has attracted attention not only because of its high-temperature properties, but also because of its high radiation stability and absorption capacity **[2.26-2.27]**.

2.1.3 Sensing properties of CeO_2

Cerium oxide (CeO_2), due to its unique ion conduction properties (oxygen vacancies), is an important material for various applications in sensor technology, fuel cells such as solid electrolytes,dsupercapacitors and oxygen sensor systems, oxygen membrane systems, refined glass materials, electronic thin layers, biotechnology **[2.28-2.29].** CeO_2 nanotubes were found to respond selectively to 100 ppm EtOH gas at an operating temperaturedofd180d°C **[2.30]**.dPreviousdstudiesdhavedreporteddtemperature-dependent selectivity of some metal oxide sensors, but the mechanisms contributing to this phenomenon remain unclear and require further investigation **[2.31–2.34]**.

Cerium oxide (CeO_2) gas for low operating temperatures **[2.35-2.38].** Limited research reports on temperature-dependent sensors in pure CeO_2 **[2.39]**. Furthermore, to our knowledge, there are no relevant studies on the relationship between gas detection and tip defects in CeO_2-based sensors. Therefore, our work here further contributes to the understanding of the factors that mainly affect the detection of CeO_2 gas sensors and to the potential exploitation of the advantages of the high catalytic properties inherent in these materials for sensor development. **[2.40]**.

2.2 Titanium dioxide (TiO_2)

2.2.1 Structural properties of TiO_2

Among the semiconductors studied, titanium dioxide (TiO_2) has excellent electrical and optical properties, low cost, non-toxicity and thermal stability compared to other metal oxides, such as SnO_2, ZnO, and is considered the most promising material **[2.41-2.43]**. TiO_2 is used as a key ingredient in industrial products such as paints, polymer products and textiles **[2.44-2.45]**.

TiO_2 exists in three crystallographic forms: anatase, rutile and brookite, but the most common polymorphs of TiO_2 are anatase and rutile, compared to anatase, rutile is more stable at high temperatures **[2.46]**. Both theoretical and experimental studies have shown that anatase TiO_2 is more suitable for solar cells than rutile due to its electronic and symbolic conductivity **[2.47]**. The formation of electron-hole pairs on TiO_2 by light irradiation with a suitable light source plays a key role in the oxidation of VOCs into CO_2 and H_2O at room temperature **[2.48-2.49]**. Other structures are under great pressure. The surface of Brookite is stable and changes to rutile at high temperatures. Technological developments and various uses of brookite have been reported.

Rutile TiO_2 is a very stable polymorph and is widely used for high temperature applications such as methane gas detection in mining **[2.50]**. Anatase TiO_2 is very stable at low temperature and transforms into rutile at high temperature. Besides being stable at the nanoscale, Anatase TiO_2 has higher photocatalytic activity and is therefore widely used in photocatalytic devices **[2.51].** Both anatase and rutile have a tetragonal $I4_1$ /

amd and $P4_2$ / mnm crystal structure, while brookite has an orthorhombic crystal structure **[2.52-2.53]**.

The unit cell contains an octahedral lattice of titanium atoms. Surrounded by 6 oxygen atoms, the lattice constants are the lattice vectors *a* and c. **[2.54-2.56]**. T- O bonds are mostly ionic with some covalent contributions. Fig. 2.1a and b show the unit cells of anatase, and rutile and Table 2.1 shows the main properties of anatase and rutile TiO_2. In anatase, the octahedron shares four edges, so the Ti atoms are at (0, 0, 0) and (0, ½, ¼) the O atom is at (0, 0, u). (0, 0, ū), (0, 0, u+) and (0, ½, ½ -u) where u = 0.305 at 15 K **[2.57]** Now, in brotyl, the Ti atoms are at (0, 0, 0) and (½, ½, ½) while the O atoms are at Atoms in ± (u, u, 0) and ±(u+ ½, ½-u, ½). Titanium oxide shares two octahedra with other octahedra and forms a combination of chains with fourfold symmetry **[2.58]**. Check **Fig.2.2** below:

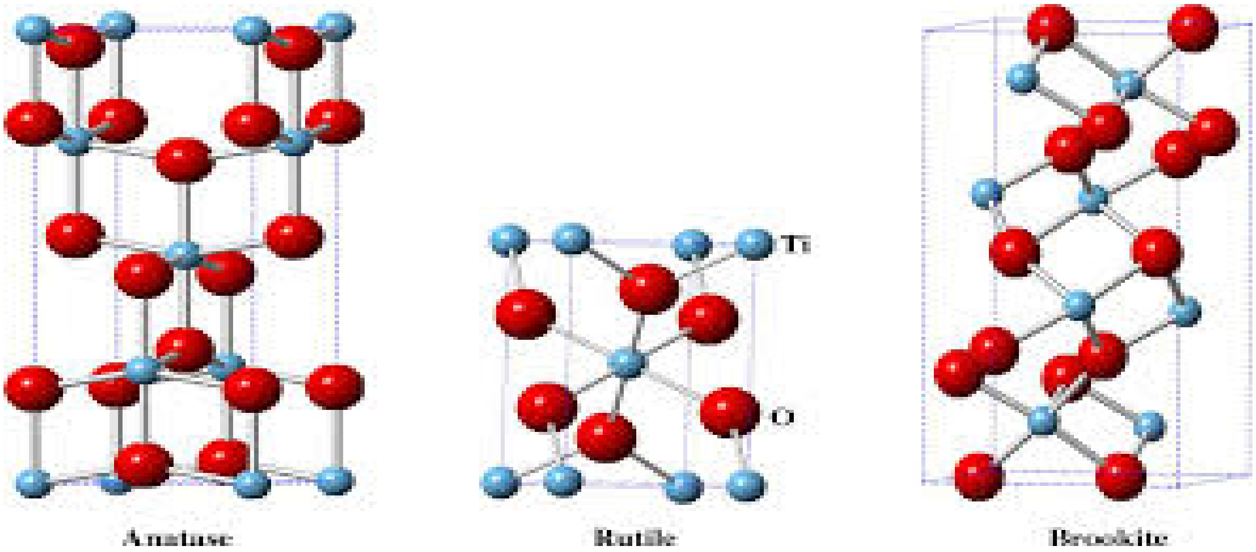

Fig. 2.2: Schematic diagram of different types of Titanium dioxide (TiO_2**)**.

2.2.2 Electrical and Optical properties of TiO_2

The anatase phase has an indirect band gap of about 3.2 eV and the rutile band gap has a band gap of about 3.0 eV **[2.59]**. Anatase is stronger than rutile. For example, oxygen molecules can be reduced to peroxide radicals. The change in stoichiometry increases oxygen vacancies (V_O) and creates Ti $^{3+}$ in the lattice. High voltage (V_O) is the reason why TiO_2 is an n-type semiconductor (see Fig.2.2) .dSuchdstoichiometricddeviationsdallowdthedcirculationdofdelectronsdanddthusdthedelectricaldconductivity of the material **[2.60]**.dThe optical propertiesdofdTiO_2 are strongly influenced by internal defect states. Oxygen vacancies, titanium vacancies and oxygen vacancies have a strong effect on the reactivity of materials **[2.61]**. Defects are good places for electron capture. TiO_2 absorbs wavelengths below 380 nm and excitation in the visible region produces photoluminescence in the green region.

2.2.3 Sensing properties of TiO_2

TiO_2 is known as one of the most valuable materials for gas analysis applications due to its non-toxicity, biocompatibility, availability, high stability and resistance to corrosion. Therefore, it works even in difficult conditions and has a long service life. Moreover, TiO_2 can be easily synthesized by various methods, such as chemical vapor deposition (CVD), anodization, electrospinning, and hydrothermal autoclave **[2.61-2.63]**. TiO_2 contains contributing defects such as oxygen vacancies and titanium vacancies that occupy the spaces between atomic sites **[2.64]**. Oxygen vacancies (V_O) form when an oxygen atom changes from its normal position to a gas state. Figure 2.5 schematically shows the detection mechanism of TiO_2 nanoparticles when exposed to oxidizing and reducing gases. When oxygen molecules are adsorbed on the surface of TiO_2, conduction band electrons and surface electrons are , O^- or O^{2-} oxygen species. This leads to bending of the ligament and an increase in the depletion layer. Since TiO_2 is n-type, oxygen ions along with the gas and surface, when exposed to reducing gases such as H_2, H_2S and CH_4, donate control electrons, creating resistance and bonds. Increases conductivity. TiO_2 exhibits the opposite behavior when exposed to oxidizing gases such as NO_x, O_2 and O_3 **[2.65 - 2.66]**.

For gas detection applications, sensitivity, selectivity, temperature and high operational stability are some of the most pressing challenges facing researchers to improve the performance of trigger sensors. Despite all the work on gas sensors, there are few reports of pure TiO_2 sensing materials with high ambient temperature (RT) sensing response and good sensitivity and selectivity. Lynn *et al*._Reference **[2.67]** report gas detection when vertically oriented TiO_2 nanotubes are synthesized by an electrochemical anodization process. The sensor responds well to formaldehyde concentrations between 10 and 50 ppm and shows good selectivity for gases such as ethanol and ammonia at room temperature.

Divya *et al* **[2.68]** reported a better response to NH_3 with a sensitivity of S = 7857 in a concentration range of 5 to 100 ppm at room temperature. The reason for this is the high surface-to-volume ratio and crystal structure of the TiO_2 permanent magnet.

2.3 Chromium oxide (Cr_2O_3)

Chromium (III) oxide (or chromia) is an inorganic compound with the formula Cr_2O_3. It is one of the main chromium oxide pigments used. In general, scholite minerals are rare. Cr_2O_3 is andinorganic compound with the chemicaldname of chromium oxide.dAlso known as dichromiumdtrioxide, chromium (3+)doxide, chromiumd(III) oxide. It usually occurs in the mineral scorlite, which occurs mainly in veins of chromium-richdskarnite,dtremolite, chloritedand metaquartzite. Chromium (III)doxide is a small hexagonal crystal of light green or dark green color. It is amphoteric and does not dissolve in water **[2.69-2.81]**.

2.3.1 Structural properties of chromium oxide (Cr_2O_3

The massdand absolute mass of thedmonoisotope of chromium (3+)doxide is 151.866dg/mol. The numberdof hydrogendbond acceptorsdis 3 and thednumber of hydrogendbondddonors is 0. Thisdcomplex is standard and includes five cooperative units. Cr_2O_3 has a dense structure consisting of oxide anions ofdthedoctahedraldholesdoccupieddbydchromium.dLikedcorundum,dCr_2O_3 is a hard and brittledmaterial (8 to 8.5 on the Mohs hardness scale). It is antiferromagnetic up to a temperature of 307 K acid resistant **[2.82]**.

2.3.2 ElectricalldanddOptical propertiesdof Chromiumdoxide (Cr_20_3)

Chromium oxide (Cr_20_3) is a semiconductor with an excess of oxygen and a high refractivedindex. Cr_20_3 films have beendstudied for optical and electronic applications such as special solar energy conversion films, solar films for windows141 and electrode materials for electronic windows 151. Attempts to increase the electrical conductivity of Cr_20_3 even with lithium, magnesium or nickel have been limited **[2.83-2.84]**.

Chromium oxide Cr_20_3 was produced by chemical vapor deposition at normal pressure, and the electrical and optical properties of the film were investigated. Chromium oxide has a wavelength between 800 and 1000 nm and absorbs wavelengths below 800 nm. The optical gap energies of the films formed at different substrate temperatures are EOpt = 2.98 to 3.09 eV. Electrical conductivity σ Cr_2O_3 between 1×10^{-2} and 2.5×10^{-3} S cm $^{-1}$ in 500K. Chromium oxide is a p-type semiconductor. At high temperature 500K the small conductivity is due to polaron jumps. For temperatures below 500K, we relate the dependence $\sigma T^{1/2}$ ddifferent frequencies **[2.85-2.86]**.

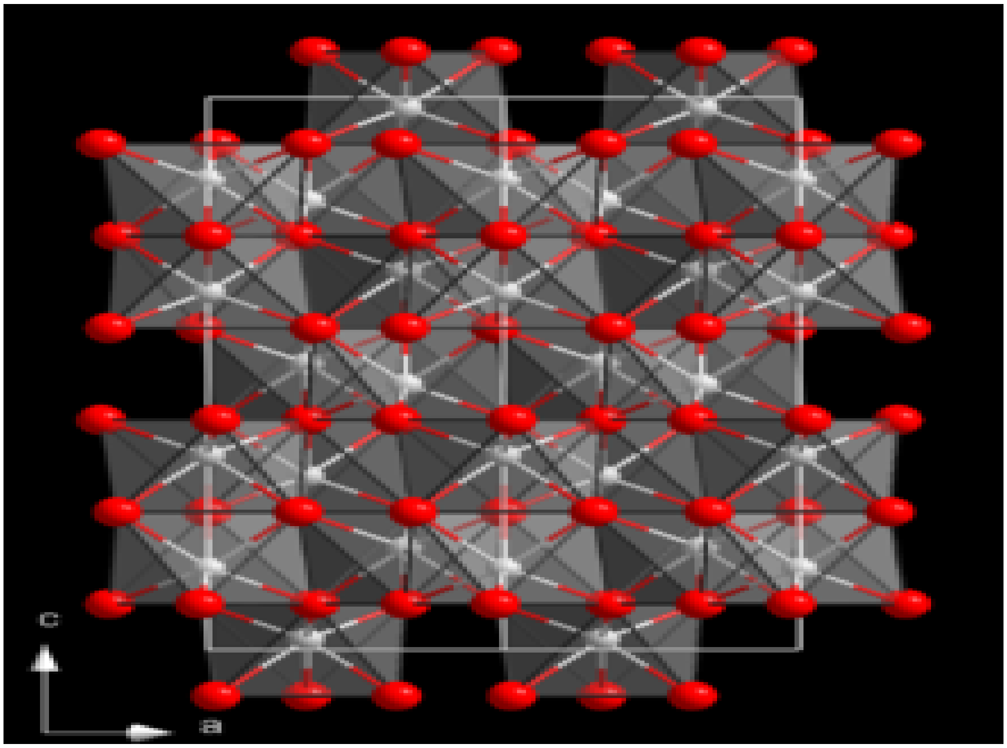

Fig. 2.3: Schematic diagram of chromium (III) oxide (Cr_2O_3) **[2.87].**

2.4. Sensor Characteristics

Currently, the most vital sensing parameters are sensor response, response and recovery times, sensitivity, selectivity, limit of detection, repeatability and stability. And these parameters are discussed below.

1. The sensordresponse (R) is defineddas the change in sensing resistance as depicted in equation 2.1 and 2.2.

$$R(\%) = \left(R_{air} / R_{gas} \right) x100$$ ……………. (2.1) Reducing gas

and

$$R(\%) = \left(R_{gas} / R_{air} \right) x100$$ ……………. (2.2) Oxidizing gas

where R_{gas} and Ra are thedresistance of thedsensor tested toward an analyte gas and Ra is the resistance in air.

2. Response and recovery times, are times needed for the resistance of the sensor to reach 90% when tested towards a target/for the resistance to reach 10% after the release of the target gas

3. Sensitivity is the rate of response to the unit of the concentration of the analyte gas.

4. Selectivity is the capability of the sensor to be able to discriminates one gas over other interfering gases.

5. Limit of detection is the lowest concentration the sensor can detect.

6. Reproducibility is number times/cycles the sensor can be able to produce the same response.

7. Stability is defined the capability of the sensor to sustain a comparatively stable and repeatable performance over a adequate period.

2.5. Current Challenges of SMO-Based Gas Sensors

Factorsdsuch asdstructure, morphologydanddsurface condition affect thedsensitive layerdand therefore thedsensor output **[2.88]**.

MOXdhasdmanydtechnicaldchallengesdthatdmakedcommercialduseddifficult,dsuchdas dlongdtermdstability/instability (ii) gasdsensitivity/cross-selectivity, dand (m)dlow/high operatingdtemperature **[2.88]**.

2.5.1. Stability

Unstable MOX undergoes transition to target gases in chemical reactions, further poisoningdthedsensordanddadverselydaffectingdthedsensord**[2.89]**.dOnedofdthedchallengesdposeddbydMOXdbaseddgasdsensors is frequent sensor replacement, unstable performance and poor stability leading to false alarms. Unless used in corrosive media, the ideal gas sensor should last longer **[2.90]**. However, the long-term reliability challenge of metal oxide sensors still remains. Sensing devices must provide stable and repeatable signals over long distances for practical use. Although MOX is limited in nanoscale particle size,dit isdhighly reactivedand prone to degradation.

Extensive research has also been conducteddto improve thedstability of MOX-baseddsensors.dHowever,dprevious studies havedshown that stabilitydcan be improved to some extent after baking **[2.91]**. Operating temperature of the lower material sensor. Compared to metal particles, metal oxides. or mixeddoxides have also been shown to improve sensordstability **[2.92]**.

2.5.2 Selectivity

Cross-sensitivity occurs when the sensor reduces the sensitivity of moisture and the interference of multiple gases in the selection environment of the sensor **[2.93]**.

Only a specific target gas molecule will be able to act as an ideal gas sensor. Unfortunately, MOX-based gas sensors seem to detect a variety of reducingdordoxidizing gases. Fordexample, da general detection sensitivityddesigned for NH_3 will respond to H_2 and CO.

If two other gases are present within the stroke monitored by the sensor, the sensor will respond as if NH_3 is present, but the other gas is also present. For implementation, the challenge of cross-sensitivity is often compounded. To find a solution to this challenge, researchers are conducting further research on newddevices that candsolve this problem,dsuchdas surface functionalization of metaldoxides withdadditives **[2.94]**.

2.5.3 Working temperature

The operating temperaturedof thedsensor determines how thedsensor reacts, as the sensitivedlayer must be heated so that the gasdmolecules are adsorbeddon the surfacedof the sensitivedlayer. In suchdconditions, the costdof sensors is increased duedto highdenergydconsumption **[2.95]**.

Theredaredthreedprocessesdondthedsurfacedofd MOXdsensors:dadsorption,ddesorptiondanddthedfunction ofdoxygen species **[2.96]**.These processes are highly temperature dependent, as thermal processes occur **[2.97]**. At lower temperatures, the results are usuallydlower,dbecausedthedgasdmoleculesddodnotdhavedenoughdthermaldenergydtodbedreflecteddwithdthedadsorbeddoxygendspecies,dwhichdslowsddowndthedchemicaldreactions.dThedresponsedalsodincreasesdwithdincreasingdtemperature,dbutdthedresponse of thedsensor is controlleddbydthe distribution ofdthe mass of gasdmolecules, so thedresponse decreases with increasing temperature. At a certain intermediate temperature, the dynamics of the two processes finally reach equilibrium and the response of the sensordreaches itsdmaximum. Researchersdhave showndthat the ultraviolet radiation from MOXdsensors reduces the temperature sensor. UVdlight is useddto induce chemicaldreactions on the surface withoutdthe need to heat the sensor, which also helps to reduce the risk of explosions and extend the life of the device **[2.98]**.

2.6 References

[2.1] Naik, J. and Bhajantri, R.F., 2018. Impact of ceria nanofillers on temperature dependent electrical and transport properties of PVA solid polymer electrolyte films. Materials Research Express, 5(6), p.065310.

[2.2] M. Gunasekaran, M. Govindhasamy, T. Rangasamy, M. K. Rangasamy and J. Ramasamy, "Facile synthesis of heterostructure Ce-O2 nanocomposites for enhaced electrochemical sensor and solar cell applications," Journal of Alloys and Compounds, vol. 773, pp. 449-461, 2019.

[2.3] N. O. D, E. M. D and C. S. H, "Gas Sensors Based on CeO_2 Nanoparticles Prepared by Chemical Precipitation Method and their TemperatureDependent Selectivity towards H_2S and NO_2 Gases," Applied Surface Science, 2019.

[2.4] T. AHMAD, M. SHAHAZAD, M. UBAIDULLAH and J. AHMED, "Synthesis, characterization and dielectric properties of TiO2–CeO2 ceramic nanocomposites at low titania concentration," Bull. Mater. Sci., pp. 41-99, 24 july 2018.

[2.5] V. S, P. R, E. S, S. T, G. G, C. Martella and L. A, "Structural, Chemical and Optical Properties of Cerium Dioxide Film Prepared by Atomic Layer Deposition on TiN and Si Substrates," Creative Commons.

[2.6] Hu, H., Liu, J., Xu, Z., Zhang, L., Cheng, B. and Ho, W., 2019. Hierarchical porous Ni/Co-LDH hollow dodecahedron with excellent adsorption property for Congo red and Cr (VI) ions. *Applied Surface Science*, *478*, pp.981-990.

[2.7] Defects and Defect Processes in Nonmetallic Solids By William Hayes, A. M. Stoneham Courier Dover Publications, 2004.

[2.8] Chanda, M., 1979. Atomic arrangements in crystalline solids. In Science of Engineering Materials (pp. 107-173). Palgrave, London.

[2.9] Black, K., 2008. Compliant substrates for materials on silicon. The University of Liverpool (United Kingdom).

[2.10] Mourdikoudis, S., Pallares, R.M. and Thanh, N.T., 2018. Characterization techniques for nanoparticles: comparison and complementarity upon studying nanoparticle properties. Nanoscale, 10(27), pp.12871-12934.

[2.11] National Center for Biotechnology Information (2022). PubChem Compound Summary for CID 73963, Cerium dioxide. Retrieved October 30, 2022 from https://pubchem.ncbi.nlm.nih.gov/compound/Cerium-dioxide.

[2.12] Smart, L.E. and Moore, E.A., 2012. Solid state chemistry: an introduction. CRC press.

[2.14] Wang, Z.L. and Kang, Z.C., 2012. Functional and smart materials: structural evolution and structure analysis. Springer Science & Business Media.

[2.15] Moore, E.A. and Smart, L.E., 2020. An Introduction to Crystal Structures. In Solid State Chemistry (pp. 1-63). CRC Press.

[2.16] V. Amita and G. J. Amish, "Structural, optical, photoluminescence and photocatalytic characteristics of sol-gel derived CeO_2-TiO_2 films," Indian Journal of Chemistry, vol. 48A, pp. 161-167, 2009.

[2.17] Z. H and B. J. F, chem.mater, vol. 14, 2002, p. 41146.

[2.18] T. RJ, Surolia PK, Kulkarni RG and Jasra R V, Sci. Technol. Adv. Mater., vol. 8, 2007, p. 445.

[2.19] A.-A. BA, Jumali MHH, Yap CC and Salleh MM, J. Nanomater, 2013.

[2.20] A. R, Mohsin M, Ahmad T and SardarM, "J.Hazard. Mater," vol. 283, p. 171, 2015.

[2.21] Klooster, W.T., Koetzle, T.F., Siegbahn, P.E., Richardson, T.B. and Crabtree, R.H., 1999. Study of the N− H⊙⊙⊙ H− B Dihydrogen Bond Including the Crystal Structure of BH3NH3 by Neutron Diffraction. *Journal of the American Chemical Society*, *121*(27), pp.6337-6343.

[2.22] Singh, G.P., Singh, J., Kaur, P., Kaur, S., Arora, D., Kaur, R. and Singh, D.P., 2020. Comparison of structural, physical and optical properties of Na_2O-Bi_2O_3 and Li_2O-B_2O_3 glasses to find an advantageous host for CeO2 based optical and photonic applications. Journal of Non-Crystalline Solids, 546, p.120268.

[2.23] El Idrissi, B., Addou, M., Outzourhit, A., Regragui, M., Bougrine, A. and Kachouane, A., 2001. Sprayed CeO2 thin films for electrochromic applications. Solar energy materials and solar cells, 69(1), pp.1-8.

[2.24] Verma, A., Joshi, A.G., Bakhshi, A.K., Shivaprasad, S.M. and Agnihotry, S.A., 2006. Variations in the structural, optical and electrochemical properties of CeO_2–TiO_2 films as a function of TiO_2 content. Applied surface science, 252(14), pp.5131-5142

[2.25] Heuer, H.W., Wehrmann, R. and Kirchmeyer, S., 2002. Electrochromic window based on conducting poly (3, 4-ethylenedioxythiophene)–poly (styrene sulfonate). Advanced Functional Materials, 12(2), pp.89-94.

[2.26] Kazazi, M., Moradi, B. and Delshad Chermahini, M., 2019. Enhanced photocatalytic degradation of methyl orange using Ag/Sn-doped CeO2 nanocomposite. Journal of Materials Science: Materials in Electronics, 30(6), pp.6116-6126.

[2.27] Shen, C.H., Wen, X.J., Fei, Z.H., Liu, Z.T. and Mu, Q.M., 2020. Visible-light-driven activation of peroxymonosulfate for accelerating ciprofloxacin degradation using CeO_2/Co_3O_4 pn heterojunction photocatalysts. Chemical Engineering Journal, 391, p.123612.

[2.28] Oosthuizen, D.N., Motaung, D.E. and Swart, H.C., 2020. Gas sensors based on CeO_2 nanoparticles prepared by chemical precipitation method and their temperature-dependent selectivity towards H_2S and NO_2 gases. Applied Surface Science, 505, p.144356.

[2.29] Kim, T.H., Kwak, C.H. and Lee, J.H., 2017. NiO/NiWO4 Composite Yolk–Shell Spheres with Nanoscale NiO Outer Layer for Ultrasensitive and Selective Detection of Subppm-level p-Xylene. ACS applied materials & interfaces, 9(37), pp.32034-32043.

[2.30] Kharton, V.V., F.M. Figueiredo, L. Navarro, E.N. Naumovich, A.V. Kovalevsky, A.A. Yaremchenko, A.P. Viskup, A. Carneiro, F.M.B. Marques, and J.R. Frade, Journal of Materials Science, 36 (2001) 1105-1117.

[2.31] Xing, L.-L., C.-H. Ma, Z.-H. Chen, and X.-Y. Xue, Applied Surface Science, 257 (2011) 8576-8580. 35

[2.32] Liao, N., M. Zhang, B. Zheng, and W. Xue, Applied Surface Science, 493 (2019) 1286-1290.

[2.33] Singh, G., Virpal, and R.C. Singh, Sensors and Actuators B: Chemical, 282 (2019) 373-383.

[2.34] Gerasimov, G.N., V.F. Gromov, M.I. Ikim, O.J. Ilegbusi, and L.I. Trakhtenberg, Sensors and Actuators B: Chemical, 279 (2019) 22-30.

[2.35] Motsoeneng, R.G., I. Kortidis, S.S. Ray, and D.E. Motaung, ACS Omega, 4 (2019) 13696-13709.

[2.36] Agarwal, S., P. Rai, E.N. Gatell, E. Llobet, F. Güell, M. Kumar, and K. Awasthi, Sensors and Actuators B: Chemical, 292 (2019) 24-31.

[2.37] Kim, T.-H., S.-Y. Jeong, Y.K. Moon, and J.-H. Lee, Sensors and Actuators B: Chemical, 2019) 127140.

[2.38] Li, Z., X. Niu, Z. Lin, N. Wang, H. Shen, W. Liu, K. Sun, Y.Q. Fu, and Z. Wang, Journal of Alloys and Compounds, 682 (2016) 647-653.

[2.39] Alali, K.T., T. Liu, J. Liu, Q. Liu, Z. Li, H. Zhang, K. Aljebawi, and J. Wang, Rsc Advances, 6 (2016) 101626-101637.

[2.40] Wang, H., Ma, J., Zhang, J., Feng, Y., Vijjapu, M.T., Yuvaraja, S., Surya, S.G., Salama, K.N., Dong, C., Wang, Y. and Kuang, Q., 2021. Gas sensing materials roadmap. Journal of Physics: Condensed Matter, 33(30), p.303001.

[2.41] Manibalan, G., Murugadoss, G., Thangamuthu, R., Kumar, R.M. and Jayavel, R., 2019. Facile synthesis of heterostructure CeO2-TiO2 nanocomposites for enhanced electrochemical sensor and solar cell applications. Journal of Alloys and Compounds, 773, pp.449-461.

[2.42] Ceria, P., 2017. CeO2-TiO2 for photoreduction of Co2 to methanol under visible light: effect of ceria loading. Malaysian Journal of Analytical Sciences, 21(1), pp.166-172.

[2.43] Yang, Y., Liang, Y., Wang, G., Liu, L., Yuan, C., Yu, T., Li, Q., Zeng, F. and Gu, G., 2015. Enhanced gas-sensing properties of the hierarchical TiO2 hollow microspheres with exposed high-energy {001} crystal facets. ACS applied materials & interfaces, 7(44), pp.24902-24908.

[2.44] R. S. Jagath, F. K. Chong and D. W. Cecilia, "CeO2-TiO2 Photocatalyst: Ionic Liquid-Mediated Synthesis, Characterization, and Performance for Diisopropanolamine Visible Light Degradation," Bulletin of Chemical Reaction Engineering & Catalysis, vol. 13, no. 1, pp. 170-178, 2018.

[2.45] Ahmad, T., Shahazad, M., Ubaidullah, M. and Ahmed, J., 2018. Synthesis, characterization and dielectric properties of $$\hbox {TiO} _ {2} $$–$$\hbox {CeO} _ {2} $$ CeO2 ceramic nanocomposites at low titania concentration. Bulletin of Materials Science, 41(4), p.99.

[2.46] Ahmad, T., Shahazad, M., Ubaidullah, M. and Ahmed, J., 2018. Synthesis, characterization and dielectric properties of $$\hbox {TiO} _ {2} $$–$$\hbox {CeO} _ {2} $$ CeO2 ceramic nanocomposites at low titania concentration. Bulletin of Materials Science, 41(4), p.99.

[2.47] Manibalan, G., Murugadoss, G., Thangamuthu, R., Kumar, R.M. and Jayavel, R., 2019. Facile synthesis of heterostructure CeO2-TiO2 nanocomposites for enhanced electrochemical sensor and solar cell applications. Journal of Alloys and Compounds, 773, pp.449-461.

[2.48] Fiorenza, R., Bellardita, M., D’Urso, L., Compagnini, G., Palmisano, L. and Scirè, S., 2016. Au/TiO2-CeO2 catalysts for photocatalytic water splitting and VOCs oxidation reactions. Catalysts, 6(8), p.121.

[2.49] Mohajan, H., 2011. Dangerous effects of methane gas in atmosphere.

[2.50] S. Sharma, M. Madou, Phil. Trans. R. Soc. A 370 (2011) 2448-2473.

[2.51] F. De Angelis, C. Di Valentin, S. Fantacci, A. Vittadini, A. Selloni, Chem. Rev. 114 (2014) 9708−9753.

[2.52] J. Muscat, V. Swamy, N. Harrison, Phys. Rev. B 65 (2002) 224112.

[2.53] F. De Angelis, C. Di Valentin, S. Fantacci, A. Vittadini, A. Selloni, Chem. Rev. 114 (2014) 9708−9753.

[2.54] U. Diebold, Surf. Sci. Rep. 48 (2003) 53-229.

[2.56] D.A.H. Hanaor, C.C. Sorrell, J. Mater. Sci. 46 (2011) 855-874.

[2.57] X. Chen, S.S. Mao, Chem. Rev. 107 (2007) 2891-2959.

[2.58] L. Kavan, M. Gratzel, S.E. Gilbert, C. Klemenz, H.J. Scheel, J. AM. Chem. Soc. 118 (1996) 6716.

[2.59] R.T. Williams, K.S. Song, J. Phys. Chem.: Solids 51 (1990) 679-716.

[2.60] J.J. Wu, C.C. Yu, J. Phys. Chem. B 108 (2004) 3377.

[2.61] G. K. Mor, O. K. Varghase, M. Paulose, C. A. Grimes, Sensor Lett. 1 (2003) 42-46.

[2.62] Y. Aykut, C.D. Saquing, B. Pourdeyhimi, G.N. Parsons, S.A. Khan, ACS Appl. Mater. Interfaces 4 (2012) 3837-3845.

[2.63] W. Zhou, H. Liu, R.I. Boughton, G. Du, J. Lin, J. Wang, D. Liu, J. Mater. Chem. 20 (2010) 5993-6008.

[2.64] C. Wang, L. Yin, L. Zhang, D. Xiang and R. Gao, Sensors 10 (2010) 2088-2106.

[2.65] H. Wua, L. Wanga, J. Zhou, J. Gao, G. Zhang, S. Xu, Y. Xie, L. Li, K. Shi, J. Colloid Interface Sci. 466 (2016) 72–79.

[2.66] S. Lin, D. Li, J. Wu, X. Li, S.A. Akbar, Sens. Actuators B156 (2011) 505– 509.
[2.67] P. Dhivya, A.K. Prasad, M. Sridharan, Ceram. Int. 40 (2014) 409-415.

[2.68] Z.P. Tshabalala, D.E. Motaung, G.H. Mhlongo, O.M. Ntwaeaborwa, Sens. Actuators B 224 (2016) 841–856.

[2.69] A. Uzunoglu, “The Use of CeO 2 -TiO 2 Nanocomposites as Enzyme Immobilization Platforms in Electrochemical Sensors,” vol. 4, no. 3, pp. 855– 868, 2017

[2.70] M. Gunasekaran, M. Govindhasamy, T. Rangasamy, M. K. Rangasamy and J. Ramasamy, "Facile synthesis of heterostructure Ce-O2 nanocomposites for enhaced electrochemical sensor and solar cell applications," Journal of Alloys and Compounds, vol. 773, pp. 449-461, 2019.

[2.71] W. S. Wu et al., “Measurement and Characterization of CeO2-TiO2 Ion Storage Films for Electrochromic Devices,” Key Eng. Mater., vol. 726, no. 3, pp. 276– 281, Jan. 2017.

[2.72] R. M. El-sherif, T. A. Lasheen, and E. A. Jebril, “Fabrication and characterization of CeO2-TiO2-Fe2O3magnetic nanoparticles for rapid removal of uranium ions from industrial waste solutions,” J. Mol. Liq., vol. 241, pp. 260–269, 2017.

[2.73] H. Abdullah, M. R. Khan, M. Pudukudy, Z. Yaakob, and N. A. Ismail, “CeO2-TiO2 as a visible light active catalyst for the photoreduction of CO2 to methanol,” J. Rare Earths, vol. 33, no. 11, pp. 1155–1161, 2015.

[2.74] M. Gunasekaran, M. Govindhasamy, T. Rangasamy, M. K. Rangasamy and J. Ramasamy, "Facile synthesis of heterostructure Ce-O2 nanocomposites for enhaced electrochemical sensor and solar cell applications," Journal of Alloys and Compounds, vol. 773, pp. 449-461, 2019.

[2.75] F. Roberto, B. Marianna, D. Luisa, C. Giuseppe, P. Leonardo and S. Salvatore, "Au/TiO2-CeO2 Catalysts for Photocatalytic Water Splitting and VOCs Oxidation Reactions," CATALYSTS, vol. 6, p. 121, 10 AUGUST 2016.

[2.76] A. Hamidah, A. I. Nur, Y. Zahira, R. K. Maksudur and A. R. Syarifah, "CeO2-TiO2 FOR PHOTOREDUCTION OF CO2 TO METHANOL UNDER VISIBLE LIGHT: EFFECT OF CERIA LOADING," MALAYSIAN JOURNAL OF ANALYTICAL SCIENCES, vol. 21, no. 1, pp. 166-172, 2017.

[2.77] M. Gunasekaran, M. Govindhasamy, T. Rangasamy, M. K. Rangasamy and J. Ramasamy, "Facile synthesis of heterostructure Ce-O2 nanocomposites for enhaced electrochemical sensor and solar cell applications," Journal of Alloys and Compounds, vol. 773, pp. 449-461, 2019. [2.160] Dey, S. and Kumar, V.P., 2021. Supported and un-supported zinc and chromium oxide catalysts for lower temperature CO oxidation: A review. Environmental Challenges, 3, p.100061.

[2.78] Motzer, W.E. and Engineers, T., 2004. Chemistry, geochemistry, and geology of chromium and chromium compounds. Chromium (VI) handbook, pp.23-88.

[2.79] Beklešovas, B. and Stankus, V., 2020. Chromium oxide synthesis by reactive magnetron sputtering and investigation. In NBCM 2020: international conference on nanostructured bioceramic materials, 1-3 December 2020, Vilnius, Vilnius University: conference book. Vilnius Univerity Press.

[2.80] Morón García, M.E., 2012. Optimizing the sintering of Cr2O3-nano powders for HVOF applications (Master's thesis).

[2.81] https://byjus.com/chemistry/cr2o3/ Accessed on 20/10/20

[2.82] Cheng, C.S., Gomi, H. and Sakata, H., 1996. Electrical and optical properties of Cr2O3 films prepared by chemical vapour deposition. physica status solidi (a), 155(2), pp.417-425.

[2.83] Lampert, C.M., 1981. Heat mirror coatings for energy conserving windows. Solar Energy Materials, 6(1), pp.1-41.

[2.84] Seraphin, B.O., 2005. Spectrally selective surfaces and their impact on photothermal solar energy conversion. Solar Energy Conversion: Solid-State Physics Aspects, pp.5-55.

[2.85] Alwan, S.T., 2021. Factors influencing the microwave propagation performance of different types of materials. Turkish Journal of Computer and Mathematics Education (TURCOMAT), 12(11), pp.736-744.

[2.86] https://en.wikipedia.org/wiki/Chromium(III)_oxide accessed on the 10/10/2022

[2.87] Gunn, G., 2014. Platinum-group metals. Critical metals handbook, pp.284-311.

[2.88] V. Bochenkov, G. Sergeev, Metal Oxide Nanostructures and Their Applications, 3 (2010) 31-52.

[2.89] M. Arafat, B. Dinan, S.A. Akbar, A. Haseeb, Sensors, 12 (2012) 7207-7258.

[2.90] N. Barsan, U. Weimar, J. Electroceram, 7 (2001) 143-167.

[2.91] E. Traversa, Ceramic Sensors for Humidity Detection: The State-of-the- Art and Future Developments. Sens. Actuators B Chem. 23 (1995) 135– 156

[2.92] T. Nitta, S. Hayakawa, Ceramic Humidity Sensors. IEEE Trans. Components Hybrids Manuf. Technol. 3 (1980) 237–243.

[2.93] S. Kurosaki, The Dielectric Behavior of Sorbed Water on Silica Gel. J. Phys. Chem. 1954, 58, 320–324.

[2.94] S. Lin, D. Li, J. Wu, X. Li, S.A. Akbar, Sens. Actuators B156 (2011) 505– 509.

[2.95] P. Dhivya, A.K. Prasad, M. Sridharan, Ceram. Int. 40 (2014) 409-415.

[2.96] Z.P. Tshabalala, D.E. Motaung, G.H. Mhlongo, O.M. Ntwaeaborwa, Sens. Actuators B 224 (2016) 841–856.

[2.97] A. Uzunoglu, “The Use of CeO 2 -TiO 2 Nanocomposites as Enzyme Immobilization Platforms in Electrochemical Sensors,” vol. 4, no. 3, pp. 855– 868, 2017

[2.98] M. Gunasekaran, M. Govindhasamy, T. Rangasamy, M. K. Rangasamy and J. Ramasamy, "Facile synthesis of heterostructure Ce-O2 nanocomposites for enhaced electrochemical sensor and solar cell applications," Journal of Alloys and Compounds, vol. 773, pp. 449-461, 2019.

CHAPTER 3

3. Characterization Techniques

3.1. Introduction

X-ray diffraction (XRD), scanningdelectrondmicroscopyd(SEM), photoluminescence (PL) and UV-vis spectroscopy, and gas testing station were utilized to investigate the structure, morphology, optical and electrical properties, such as change in sensor resistance.

3.2. X-ray diffraction

X-ray diffraction (XRD) technique is utilized to probe the structure, crystallite sizes, lattice parameters and strain of the materials. It is created on the x-rays beam incident on a material, see **Fig. 3.1**. The atoms in the materials create a diffraction of the incident beam of X-rays into numerous precise directions. Depending on the wavelength, incident and scattering angles, these waves will cancel one another out via a destructive interference, or they add constructively in specific directions administered by Bragg's law (equation 3.1) **[3.1]**. Each crystalline material contains an exclusive XRD pattern to recognize its crystal structure. The obtained XRD patterns may represent the arrangement and orientation of a specific set recognized by Miller indices (*h*, *k*, *l*) **[3.2]**.

$n\lambda = 2d\sin\theta$………………………….. (3.1) where n is an integer almost equal to 1, λ =d1.5418 Å isdthe uniformity ofdthe emitted beamdCu K *a ,* d isdthe grating spacedbetween the diffraction planesdand θ thedangle ofdincidence.

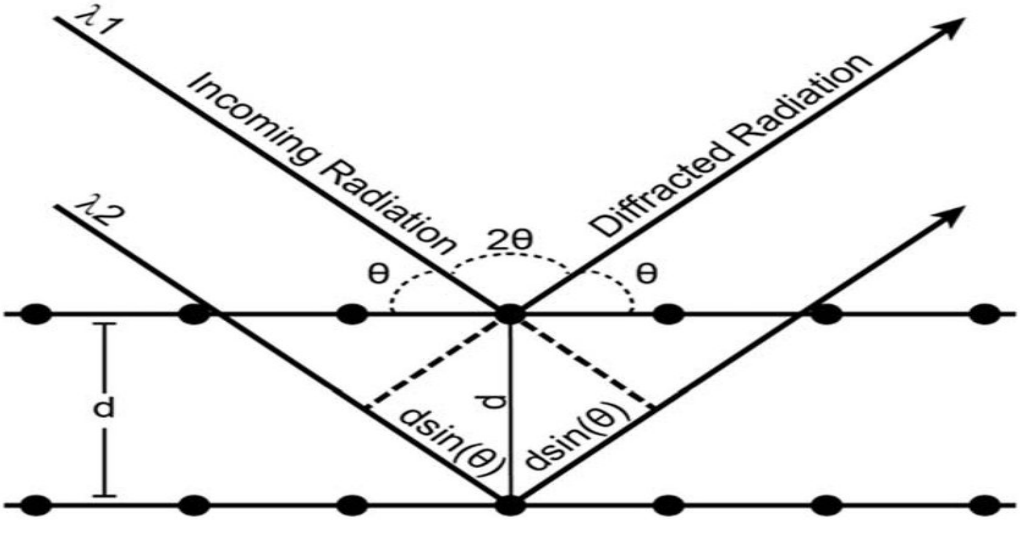

Fig. 3.1:dSchematic drawing showing the diffractiondpatterns according to Bragg'sdlaw **[3.2]**

Whendexaminingddiffractiondpatterns, the peak widths and intensities at full widths at half maximum (*b* measured radiation) are useful in determining the crystallite size (L) of the Debye-Scherrer pattern of Eq. 3.2 **[3.3-3.4]**.

.... (3.2)

where *K is* a constant = 0.94.

We also propose a model based on the well-known Williamson-Hall method as presented in ref. **[3.4]**. It takesdinto accountdthe distortions (*e)* caused by the crystalline imperfectionsdand latticedmodes.

.... (3.3)

Rearranging equation 3.3 gives:

…………………………….(3.4)

In this study, a Bruker AXS D8 Advance x-ray diffractometer, Cu Kα radiation λ= 0.154056) XRD was used to study the properties of the materials.

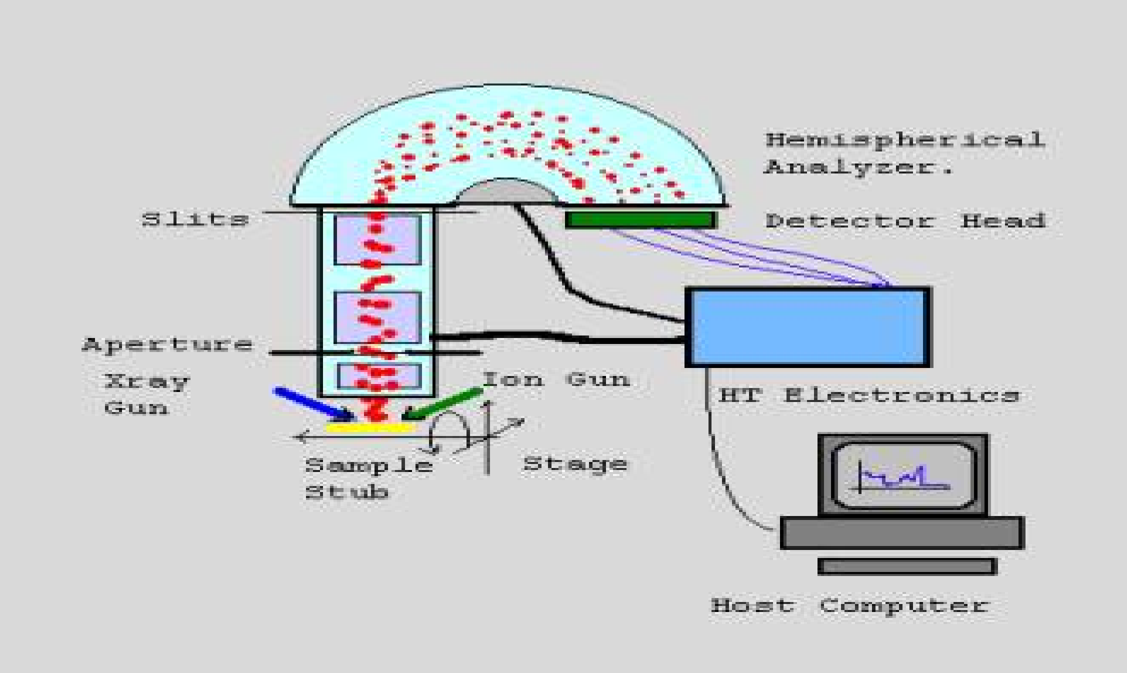

Fig.3.2: Schematicddiagramdof an X-raydspectrometer **[3.5].**

3.3. Scanning ElectrondMicroscope

Electrons are emitted by a scanningdelectron microscoped (SEM)dfrom the emission field indandelectrondgundatdthedtopdofdthedcolumn.dElectrons are concentrated by electromagnetic lenses, gyres and slits (objective lenses and condensers) to guide the electron cloud. Electrons are excited by high voltage (5-20 kV) in a vacuum in a thindprobedthatdscansdthedsurfacedofdthedmaterial. Admagnetic field is often required to create and control the beam. As shown in **Fig. 3.2**, when an electron beam intersects a sample, it loses energy in a different way than a given sample. Any lost energydemitted asdsecondarydelectronsd(low energy), demitted electronsd (highdenergydor X-rays (see **Fig. 3.3**) is converted into heating **[3.6]** . They are converted into signals by the detector and adjusted to theDscreen intensitydcorrespondingdtodthedpositiondofdthe beamdin thedsample. In addition,dthe emittedSX-raysdaredcharacteristicdofdthedatomsdindEnergyvDispersivedX-raydSpectroscopyd(EDS).

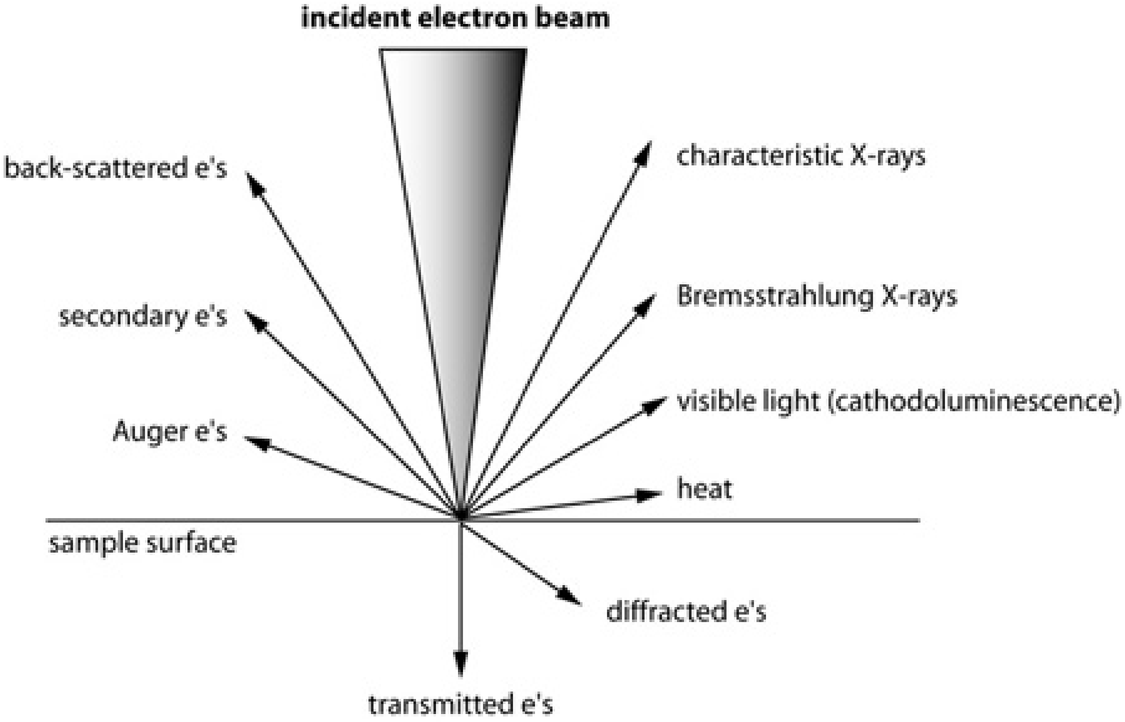

Fig. 3.3.dElectron-specimendinteraction **[3.7].**

Resolution of the camera,dworking,vdistancedanddsphericaldaberration affect imagedquality anddfocus **[3.8]** . The sample is coated with a conductive layer (often called saturation) in preparation for the non-conductive image acquisition. Excess electrons accumulate and are released in rapid bursts, distorting the image unless properly covered.

The electrical coating improves electrical conductivity and secondary and repulsive electron emission, and limits damage to the sample from excessive radiant heating. For the current study, Zeiss scanning electron microscope (SEM, 3kV EHT, Zeiss) was used to probe the surface morphology.

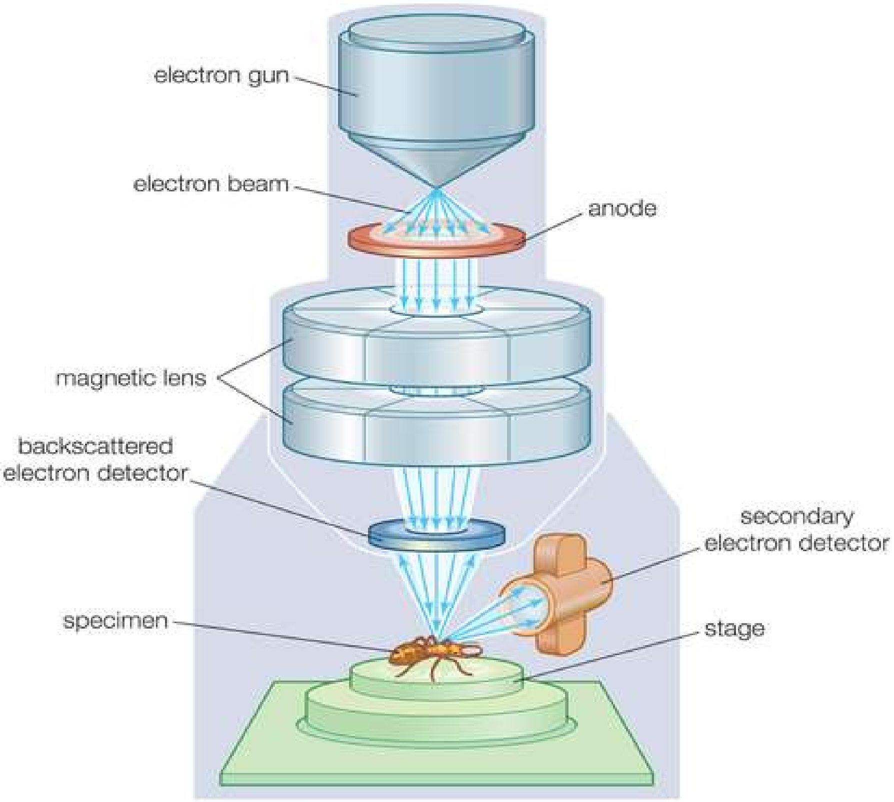

Fig. 3.4: Schematicddiagram showing the SEM setup **[3.9]**

3.4. PhotoluminescenceDspectroscopy

PhotoluminescenceD(PLDspectroscopyDisDanDimportantDtechnique for theDanalysis of defectiveDsurfaceDstates,DdonorDandDacceptorDstates,Dand for the trap states induced in the bulk material. When a photon is absorbed by a material, electrons with valence energies equalDtoDorDgreaterDthandthedbanddgapdofdthedmaterial are excited and enter the conduction band. By reducing the energy emitted by a photon perceived as light, the excited electron returns to its original state **[3.10].** Whether a material has direct or indirect bonds greatly affects the photon absorption process.

Front band: Electrons absorb the energydanddmomentum of the incident photondwithout changingdthe wavevectordand enter thedconductiondband vertically. ElectronsdandDholesdaredformeddindthedconductiondanddvalencedbands,drespectively.dHowever, because an excited electron needs extra energy in the oblique material to enter the beam, the transfer involves one phonon into the other to maintain momentum **[3.11]** . It loses its excitation energy and emits another photon during the relaxation process. The PL spectrum shows the change of excited states filled with excitations. Radiation recombination between excitons and electron-coulomb-bonded pairs can be explained **[3.12]**. In this study, room temperature photoluminescence (PL, spectrometer with a Kimmon IK series 325 nm laser) spectroscopy was utilized to probe the surface defects of the materials.

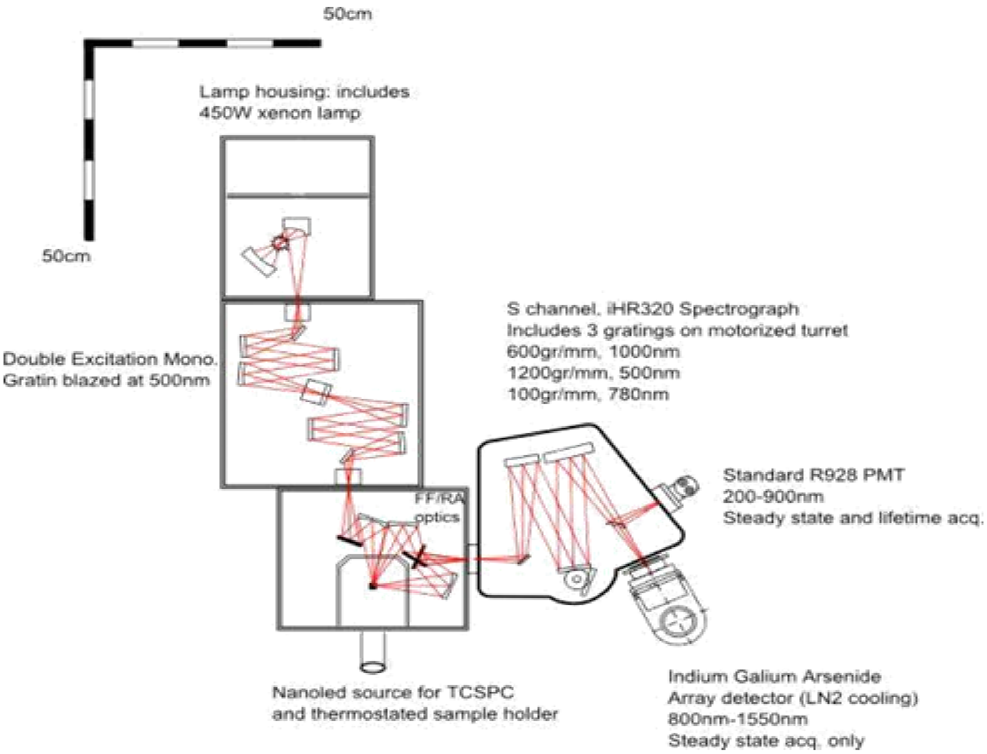

Fig. 3.5: Schematic diagram showing the NanoLog PL spectrometer **[3.13].**

3.5 Ultraviolet-visible (UV-vis) spectroscopy

UV-vis spectrometry is utilized to analyze the sample's transmittance, reflectance, and absorption. When the sample is optimally treated with electromagnetic radiation of different wavelengths (near UV and near IR), one may get a UV-vis spectrum. Consequently, monochromatic radiation is used at once. The spectrum is the ratio of the amount of energy absorbed at each wavelength to its wavelength **[3.14]**.

The location of the greatest absorption band, known as -max, and the intensity of the absorption bands are the two most important metrics used to characterize the UV spectra of compounds **[3.15]**. Using UV-vis data, even the energy band gap of the materials may be estimated. Figure 3.13 is a schematic illustration of how a UV-vis spectrophotometer produces data.

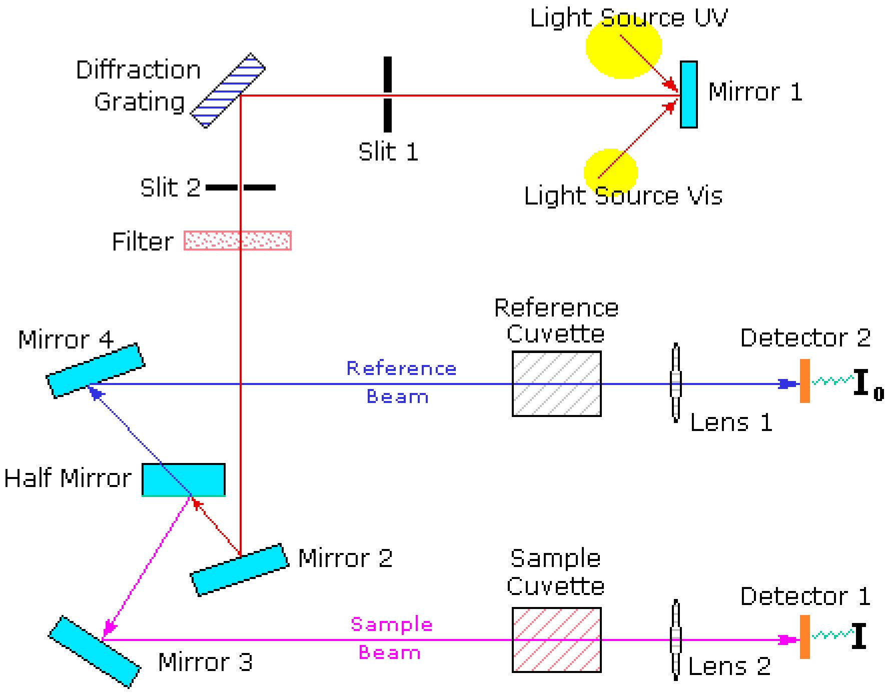

Fig. 3.6: The schematic diagram of UV-visible spectrophotometer (UV-vis) **[3.16].**

3.6. Gasdtestingdstation

The sensors performance was assessed using a commercial 4-channel Gas Mixing System (GMS) sensing equipment, see **Fig. 3.6 [3.17]**. Prior to measurements, few grams of CeO_2, TiO_2, CeO_2-TiO_2, CeO_2/TiO_2, $Cr_2O_3/TiO_2/CeO_2$ and $Cr_2O_3/CeO_2/TiO_2$ nanostructured materials were mixed with ethanol and grinded in a mortar to form a paste, which was homogenously spread over the interdigital electrodes. The paste was dried for 10 hours at 80 °C to attain a proper adhesion. The fabricated-based sensors were placed in a Teflon chamber and tested for various gases, including ethanol, carbon monoxide, methane (CH_4), carbon dioxide (CO_2), and nitrogen dioxide (NO_2). The measurements were carried out at various operational temperatures (25, 50., 75, 100, 150, and 200 °C). The sensors were initially exposed to dry air for 3 h to sustain the resistance during the measurements. Thereafter, the sensors were exposed to the analyte gases for 20 min, and dry air was introduced for 40 min for proper recovery. The sensors were tested in dry air and relative humidity conditions. The sensing response was specified as R_a/R_g and R_g/R_a, for the reducing and oxidizing gas, respectively, denoting the resistance ratio of the sensor exposed to air (R_a) and the tested gases (R_g).

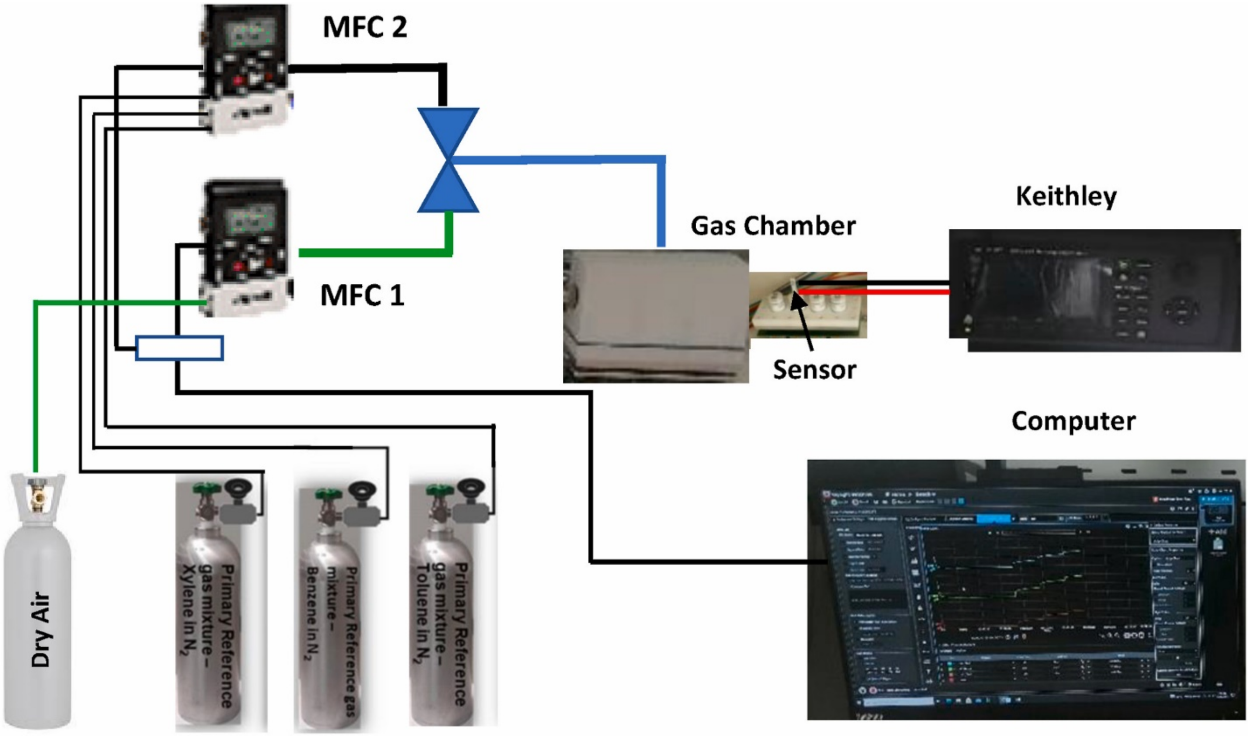

Fig. 3.7: Schematic diagram showing the gas sensing used in the current thesis **[3.17].**

3.7 Hydrothermal Synthesis method

Hydrothermal synthesis can be defined as a method of synthesis of single crystals that depends on the solubility of minerals in hot water under high pressure. The crystal growth is performed in an apparatus consisting of a steel pressure vessel called an autoclave, in which a nutrient is supplied along with water. A temperature gradient is maintained between the opposite ends of the growth chamber. At the hotter end the nutrient solute dissolves, while at the cooler end it is deposited on a seed crystal, growing the desired crystal **[3.18]**.

The CeO_2-TiO_2 was synthesized using the following three routes, our first step we fabricated CeO_2 by 5 ml of 0.4 mol/l $Ce(NO_3)_2$ solution which will be slowly dropped into 35ml of 9 mol/l NaOH solution while stirring fast and after the solution was be placed in a 50 ml Teflon-lined stainless steel autoclave for it to be cooked at 120 ^{0}C for 24 h, after the stainless steel was taken out to cool under the temperature of 25^{0}C. Along the process, the preciptates were brought apart by centrifugation, cleaned by distilled water and also ethanol, and kept in air to dry. Secondly, we prepared TiO_2, by adding 25 ml of a 0.2mol/l $Ti(SO_4)_2$ aqueous solution into the suspension for 1 hour and half under 30 ± 5 ◦C, after the solution was stirred in the very same temperature for 3 hours more and then it was kept in room temperature for 2-3h for it to cool down, then precipitate were washed with distilled water and also ethanol and brought apart by centrifugation, it was dried in air. Thirdly, the obtained products (CeO_2 and TiO_2) will be mixed at 360 ◦C for 6 hours with Ar/H_2 and then at 600 ◦C for 2 h in the ambient atmosphere. You can check on fig 3.8 below, which shows the steep that need to be followed:

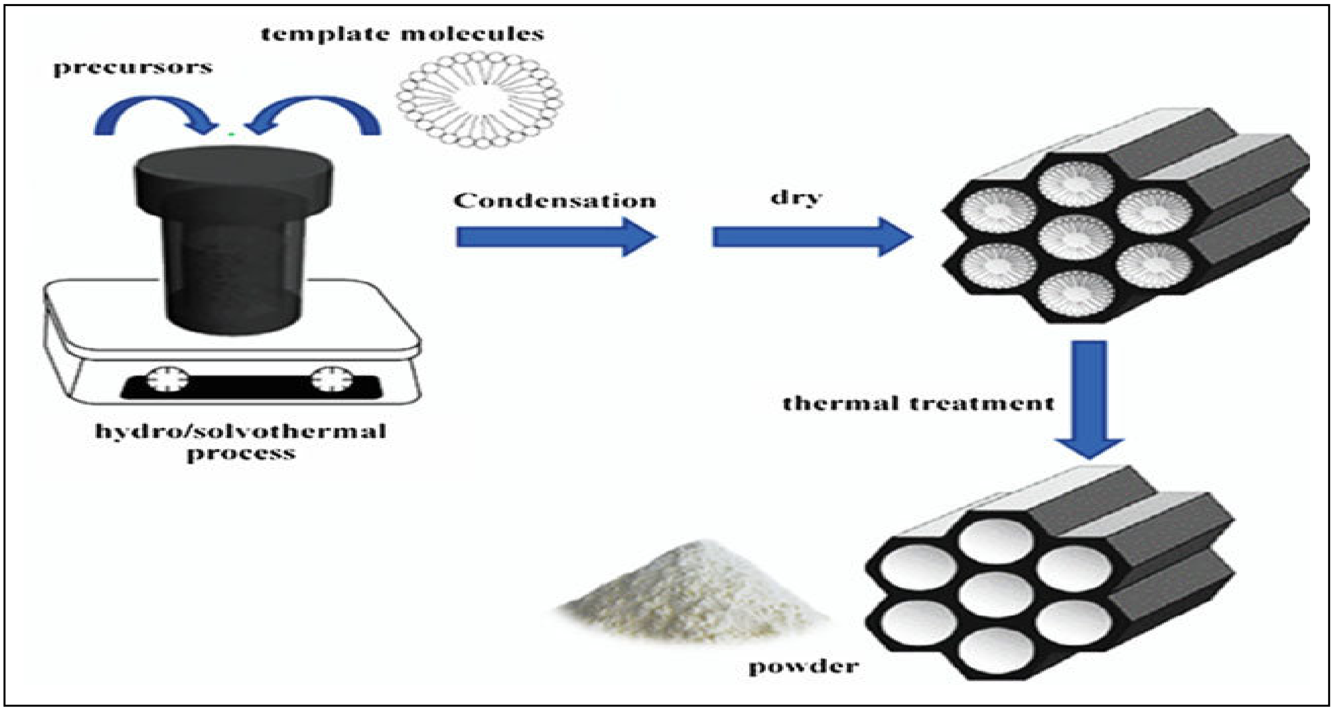

Fig. 3.8: Schematic diagram showing the hydrothermal synthesis method [3.19].

3.9 Sol-gel Synthesis method

This one of methods to synthesis metal mixed oxide, where the whole process starts by formation of a metal alkoxide in solution. Dispersed colloid known as a “sol” has been formed through the process of hydrolyses of metal alkoxide and it procedure to form “gel’ through polycondensation. The last step it was for us to form a metal oxide by calcinating the gel which is dried, to ensure that all the solvents are removed which can cause the formation of a porous gel such as xerogel or aerogel **[3.20]**.

In the case of Sol-gel method at room temperature, the typical experimental procedure to synthesize CeO_2-TiO_2 was as follows: Firstly, Titanium oxide gel was prepared following this steps: 10mL of Titanium tetraisopropoxide was used as a precusor and it was mixed with 30mL Ethanol then the solution was stirred for 60 min at the temperature of 60 ^{0}C at 300 rpm. While waiting for 60 min to elapse, the solution of 3mL of HNO_3 and 150mL Distilled water was prepared aside and it was used to titrate the first solution dropwise for 2 hours at 60^{0}C. Secondly, Cerium oxide gel was prepared following this steps: Cerium nitrate was used as a precursor where, 10 mL of ($Ce(NO_3)_3$) was mixed with 1mL of Ethanol and 1 mL of ammonium then the solution was stirred for 60 min at the temperature of 60 ^{0}C at 300 rpm. Two solutions of Titanium oxide and Cerium oxide in gel form were be mixed, and placed in a microwave oven for 24h at 100^{0}C. After the it was annealed for 24 hours at 80^{0}C, 120^{0}C, 200^{0}C, 300^0 C to form CeO_2-TiO_2 powder. You can check on fig 3.9 below, which shows the steep that need to be followed:

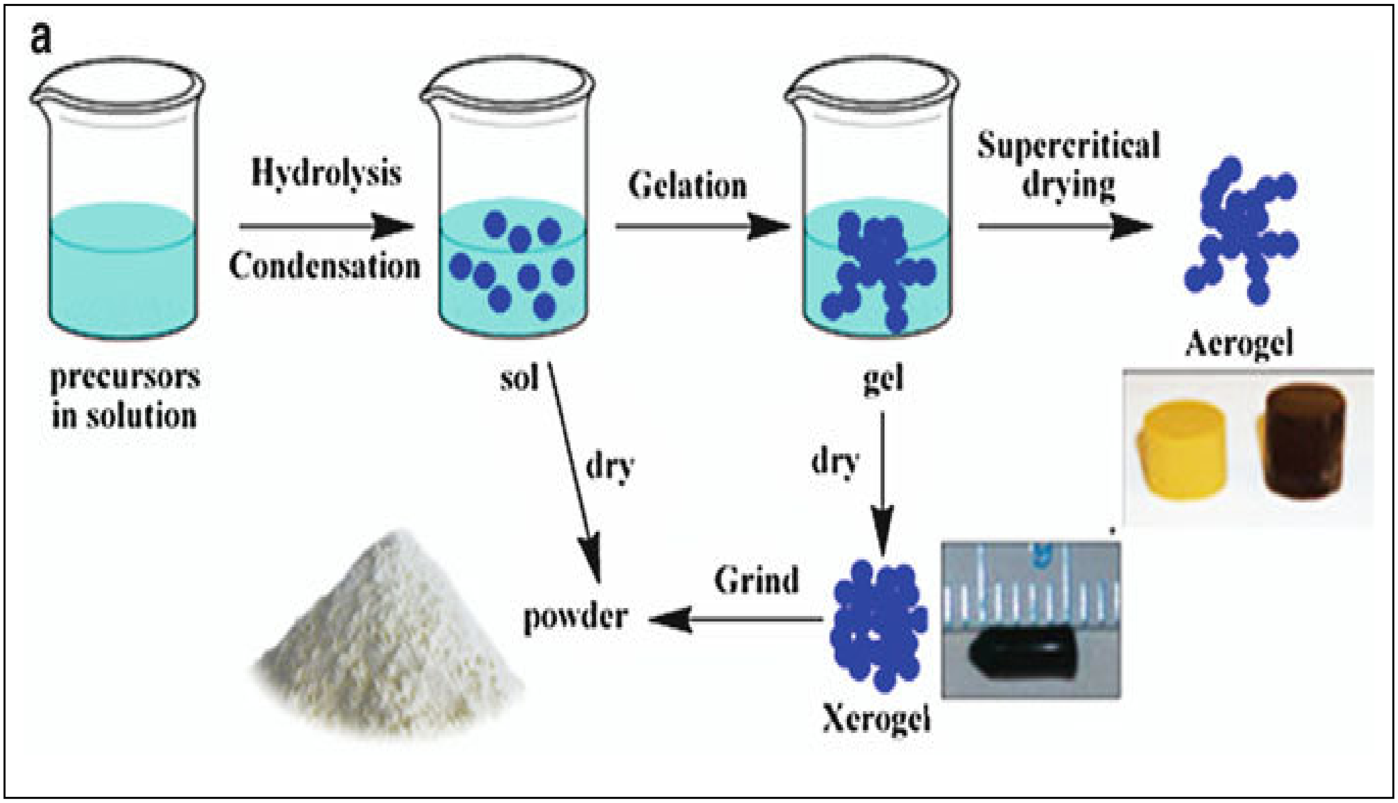

Fig. 3.9: Schematic diagram showing the sol-gel synthesis method [3.21].

3.7 References

[3.1] B. Fultz, J. Howe, Springer (2003).

[3.2] Comic Culture , Addison Wesley, (1956).

[3.3] JR Connolly, EPS400-002, Springer (2007)

[3.4] BR Rehani, PB Joshi, KN Lad, A. Pratap, Indian J. Pure & App Physics_44 (2006) 157-161.

[3.5] CV Raman, KS Krishnan, Indiana J. Phys., 2 (1928) 387-398.

[3.6] http://fluorescence.ttk.pte.hu/nanologseminar2013/devices.php

[3.7] P.L. Hall, Clay Minerals 15 (1980) 321-335.

[3.8] DM Murphy, Chapter 1, WILEY-VCH Verlag GmbH & Co. KGaA , Weinheim (2009).

[3.9] J. Weil and J. Bolton, 2nd ed. J. Wiley, USA (2007).

[3.10] K. Siegbahn, AI Edvarson , Nuclear Physics 1(8) (1965) 137-159.

[3.11] A.Einstein, Ann. Physics 17 (1905), 132. 1921 Nobel Prize in Physics.

[3.12] Iris and Wolfgang E. S. Unger, 7 (2003) 519.

[3.13] LC Feldman, JW Mayer, (1986).

[3.14] http://www.chem.qmul.ac.uk/surfaces/scc/scat5_3.htm (accessed 28 November 2020)

[3.15] J. I. Pankove, Optical process in semiconductors, Prentice-Hall: New Jersey,

[3.16] M.S.Pradeep Kumar Patnaik, K.Rama Kumara Teja and Y.Haritha, “Spectrophotometric determination of organic samples,” International Journal of Current Engineering and Scientific Research (IJCESR), vol. 2, pp. 40- 43, 2015.

[3.17] Lekgolo M Maebana, Zamaswazi P Tshabalala, Hendrik C Swart, Nompumelelo Leshabane, Lucas JB Erasmus, David E Motaung, Comparison study on ZnO and CuO gas sensing characteristics: Temperature modulated-dual selectivity towards benzene and xylene vapours, Materials Chemistry and Physics 297 (2023) 127352.

[3.18] Kharisov, B.I., Kharissova, O.V. and Mendez, U.O., 2012. Microwave hydrothermal and solvothermal processing of materials and compounds. *The Development and Application of Microwave Heating*, *5*, pp.107-140.

[3.19] https://www.researchgate.net/figure/Schematic-view-of-a-sol-gel-reaction-and-b-solvo-hydrothermal-synthesis-of_fig2_286576071 Accessed (27/06/2023).

[3.20] Niederberger, M. and Garnweitner, G., 2006. Organic reaction pathways in the nonaqueous synthesis of metal oxide nanoparticles. *Chemistry–A European Journal*, *12*(28), pp.7282-7302.

[3.21] https://www.researchgate.net/figure/Schematic-view-of-a-sol-gel-reaction-and-b-solvo-hydrothermal-synthesis-of_fig2_286576071 Accessed (27/06/2023).

CHAPTER 4

Structure, and optical properties of CeO_2, TiO_2, and TiO_2-CeO_2 nanostructures

4.1 Introduction

Semiconductor metal oxide-derived gas sensors have attracted much attention due to their rapid response/recovery times, low limit of detection, superior sensitivity, and selectivity towards target gases [**4.1-4.3]**.

Amongst the semiconductors that have been studied Titanium oxide (TiO_2) has been considered the most promising semiconductor because of its superior optical and electrical characteristics, high chemical stability, catalytic activities, high sensitivity, fast response, low cost, not poisonous and high electric constant**,** compared with the other n-type semiconductor metal oxides such as WO_3, ZnO, In_2O_3, Fe_2O_3, and SnO_2 **[4.4-4.7]**.

Titanium oxide (TiO_2) exist in three forms which are anatase, rutile and brookite crystallographic, the most popular polymorphs of Titanium oxide (TiO_2) are anatase and rutile form since brookite is rather unstable where rutile form is the most stable at higher temperature compared to anatase form. It has been reported that various phases have a strong influence on the sensing and catalytic activity properties of TiO_2 **[4.8-4.14]**.

On the other hand, cerium oxide (CeO_2) has also attracted significant attention because of its exceptional properties, which tend to produce higher surface defects, like oxygen vacancies, which play an excellent role in sensing performance [**4.15-4.16]**.

To improve the gas sensing performance of metal oxide semiconductors, studies have shown that mixed metal oxide semiconductors, can be effective in sensing characteristics due to their high surface area and reactive sites. As a result, the current project attempts to use CeO_2-TiO_2 mixed metal oxides as a gas sensing layer for the detection of CH_4 gas.

Thus, in the current chapter, we discuss the structure, morphology, and optical properties of pure CeO_2, TiO_2, and mixed CeO_2 -TiO_2 heterostructure. In terms of sensing performance, the pure CeO_2, TiO_2, and mixed CeO_2 -TiO_2 displayed higher sensing resistance leading to poor sensing signals, therefore no sensing results are displayed in this chapter. Such poor sensing performance could be justified probably by the adopted synthesis method. Generally, studies have reported that mixed oxides lead to improved sensing performance **[4.17, 4.18].** Therefore, in chapter 5, a different approach to synthesizing various nanostructures was adopted. Basically, Cr_2O_3 was loaded on the CeO_2 and TiO_2 surfaces.

4.2. Experimental Details

4.2.1. Chemicals

Titanium tetraisopropoxide (TTIP); Ethanol; Distilled water; Nitric acid (HNO_3); Cerium Nitrate ($Ce(NO_3)_3$); Ethanol and Ammonium.

4.2.2. Synthesis procedure of CeO_2 nanoparticles

Sol-gel method was used to synthesize Cerium oxide (CeO_2) as follows: Cerium nitrate was used as a precursor where 10 mL of ($Ce(NO_3)_3$) was mixed with 1mL of Ethanol and 1 mL of ammonium then the solution was stirred for 60 min at the temperature of 60 ^{0}C at 300 rpm. The solutions of Cerium oxide in gel form were mixed and placed in an oven for 24h at 80°C, 120°C, 200°C, and 300°C to form CeO_2 powder.

4.2.3 Synthesis procedure of TiO_2 nanoparticles

Sol-gel method was used to synthesize Titanium dioxide (TiO_2) metal oxide as follows: Firstly, Titanium oxide gel was prepared using 10mL of Titanium tetraisopropoxide was used as a precursor and it was mixed with 30mL ethanol then the solution was stirred for 60 min at the temperature of 60°C at 300 rpm. A separate beaker, with the solution of HNO_3 and distilled water, was prepared aside, and it was used to titrate the first solution dropwise for 2 hours at 60°C. Lastly, the solution of Titanium dioxide (TiO_2) in gel form was placed in an oven for 24h at 80°C, 120°C, 200°C, and 300°C to form TiO_2 powder.

4.2.5. Synthesis procedure of CeO_2-TiO_2 nanoparticles

Sol-gel method was used to synthesize CeO_2-TiO_2 mixed metal oxides as follows: Firstly, Titanium oxide gel was prepared using 10mL of Titanium tetraisopropoxide was used as a precursor and it was mixed with 30mL ethanol then the solution was stirred for 60 min at the temperature of 60°C. A separate beaker, with the solution of HNO_3 and distilled water was prepared aside, and it was used to titrate the first solution dropwise for 2 hours at 60°C.

Secondly, CeO_2 gel was prepared using 10 mL of (Ce $(NO_3)_3$) was mixed with 1mL of ethanol and ammonium then the solution was stirred for 60 min at the temperature of 60°C.

Lastly, two solutions of CeO_2 and TiO_2 in a gel form were mixed and placed in an oven for 24h at 80°C, 120°C, 200°C, and 300°C to form CeO_2-TiO_2 mixed metal oxides powder.

4.2.6. Characterization

The structure was investigated using the X-ray diffraction (XRD, Bruker AXS D8 Advance x-ray diffractometer, Cu Kα radiation $\lambda = 0.154056$). Scanning electron microscope (SEM, 3kV EHT, Zeiss) was used to probe the surface morphology. Room temperature photoluminescence (PL, spectrometer with a Kimmon IK series 325 nm laser) spectroscopy was utilized to probe the surface defects of the materials.

UV-vis spectroscopy was used to probe the absorption spectra and optical bandgap of the materials.

4.3. Results and Discussion

The X-ray diffraction patterns of as-prepared CeO_2 nanoparticles at various temperatures from 80°C to 300°C are shown in **Fig. 4.1 (a)**. The distinctive peaks are remarkably similar to the fluorite crystal structure of CeO_2 **[4.17, 4.18]**, with preferred development along the (101), (111), (200), (220), (311), (222), (400), (331), (420), and (422) planes corresponding to 2θ = 28,3°, 32,9°, 47,3°, 56,2°, 59,0°, 64,5°, 76,7°, 79,2°, and 88,4°. No additional phase peaks were seen, suggesting the product's excellent purity. Additionally, the observed diffraction peaks of CeO_2 are relatively broad, indicating that the sample crystalline sizes are small. The diffraction peak patterns found were compared to JCPDS standard diffraction values (Card Nos. 00-004-0593).

The XRD patterns in **Fig. 4.1(b)** affirm the existence of pure TiO_2 nanostructure. The observed peaks were linked with JCPDS data (00-002-0406) for the anatase phase and (00-002-0494) for the rutile phase, the peaks attained in the pattern coincide perfectly with the pure TiO_2. The high intensity of the peaks shows that samples have a good crystalline nature. The strong diffraction peak around 25.35° and 48.08° indicates TiO_2 is in the anatase phase at 80°C and 120°C, while the rutile peaks positioned at 27.52°; 36.23°and 41.21°, corresponding to (110); (101); and (111) respectively were detected at 200°C and 300°C. **[4.17, 4.18]**. The anatase phase was retained at low temperatures. The phase change to anatase-rutile was detected when the temperature was raised to 80°C and 120°C. This indicates that anatase stabilization or anatase–rutile transition occurs at a greater temperature.

XRD patterns of the CeO_2-TiO_2 mixed metal oxides are shown in **Fig. 4.1(c).** The peaks at 28.738°, 33.255°, 47.803°, and 56.745° correspond to typical CeO_2 fluorite structure reflections (JCPDS 34-0394). An extra peak linked to the TiO_2 anatase phase was discovered by XRD at 25.34° (JCPDS No: 21-1272). This meant that Ti^{4+} ions injected into the CeO_2 lattice created a substitutional solid solution, which is advantageous for improved sensing properties. The metal oxide system's nanoscale crystalline size was revealed by the wide XRD peaks. The expansion of crystallite size is influenced by increasing the sample's temperatures from 120°C to 300°C with the decreasing broadening of the diffraction (β) and decrease in strain, as seen in Table 1 and Figure 1 (c). From **Fig. 1c**, we noticed that cerium dominates in CeO_2-TiO_2 mixed metal oxides, and the highest peak observed is from Cerium oxide, which means that the crystal size of the mixed metal oxide is determined by (111) peak, from CeO_2. This behaviour is consistent with the previous reports **[4.18, 4.19].**

The crystallite sizes were calculated using the Debye-Scherer formula **[4.18]**. The crystallite size reduced as the temperature increased, as seen in Table 4.1. Table 4.1 shows the lattice parameters a, c, and the volume of the unit cell (v), which was calculated using Vergard's rule **[4.19]**. As the temperature rises, the lattice parameter a contract, whereas lattice *c* increases, suggesting lattice growth. The expansion of the lattice is caused by a rise in temperature inside the interstitials. Although rutile is present in the 200°C and 300°C samples, the lattice characteristics do not, owing to the dominance of the anatase phase (see Table 4.1). As the temperature increases from 80°C to 120°C anatase phase, the strain remains the same, and at 200°C and 300°C the strain decreases, and the Crystallite size increases at the anatase-rutile phase as the temperature increases and the broadness of the peak also decreases.

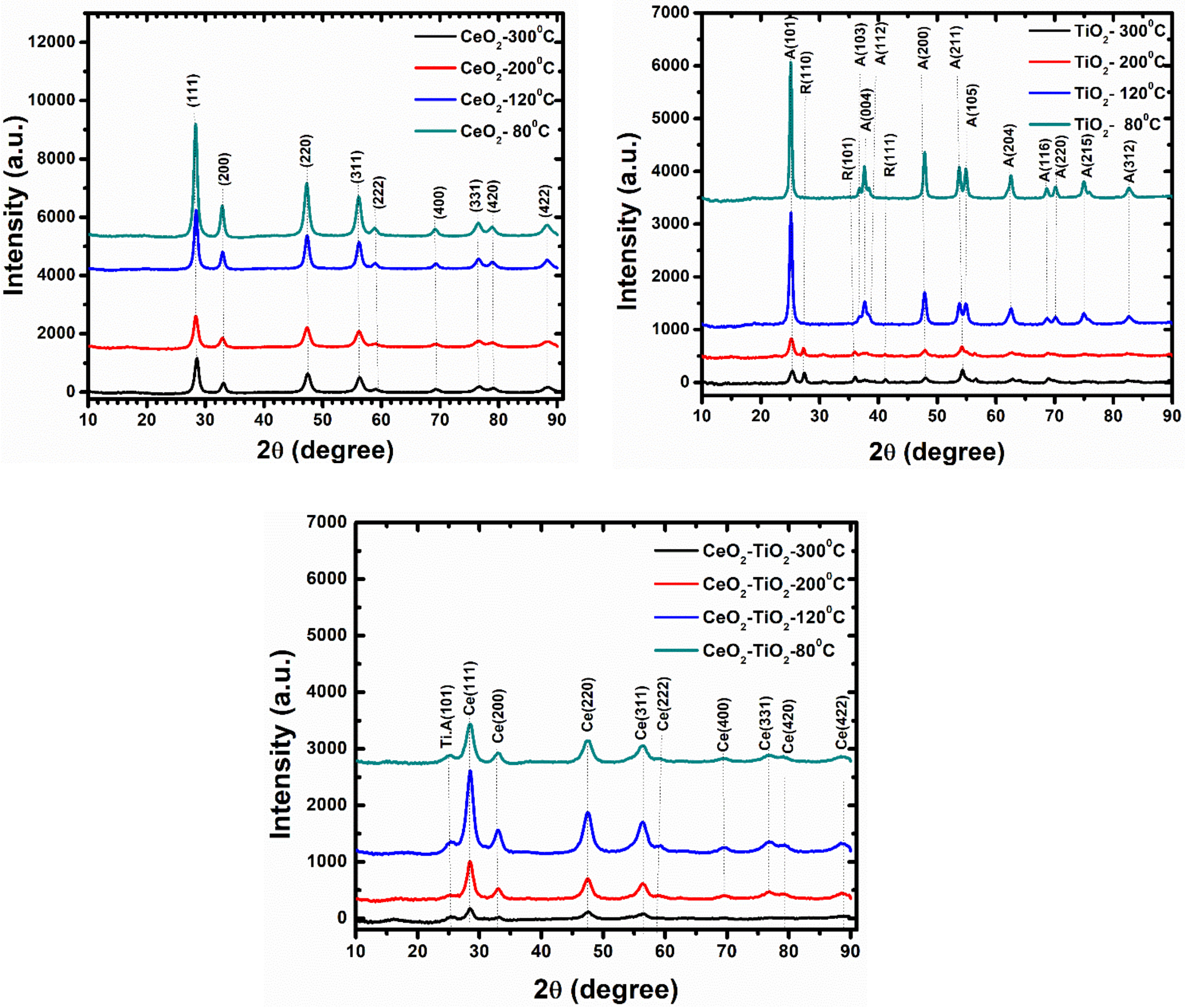

Fig. 4.1: XRD patterns of the (a) CeO$_2$, TiO$_2$ and mixed metal oxides CeO$_2$-TiO$_2$ heterostructure**.**

Table 4.1: Summary of d-spacing, crystallite size, strain, and lattice parameters of CeO2 at different synthesis temperatures.

Sample	**2θ(°)**	**d_{111}(nm)**	**D_{111}(nm)**	**Strain**	**a (nm)**	**V $(nm)^3$**
Pure CeO_2	28.550	0.3124	10,4439	0.0034	0.5411	0.1584
80°C	28.3206	0.3149	10.4386	0.0035	0.5448	0.1617
120°C	28.3936	0.3140	10.9624	0.0033	0.5435	0.1606
200°C	28.3638	0.3144	7.8690	0.0046	0.5443	0.1613
300°C	28.5220	0.3127	9.2656	0.0039	0.5417	0.1590

Table 4.2: Summary of d-spacing, crystallite size, strain, and lattice parameters of TiO_2 at different synthesis temperatures.

Sample	**2θ(°)**	**d_{101}(nm)**	**D_{101}(nm)**	**Strain**	**a (nm)**	**c (nm)**	**V $(nm)^3$**
80^{0}C	25,0952	0.3546	19,57037824	0,0019	0.3798	0.9896	0.1428
120^{0}C	25.0952	0.3546	19,18131929	0,0019	0.3798	0.9547	0.1377
200^{0}C	25.1028	0.3545	8,077654249	0,0045	0.3792	0.9971	0.1434
300^{0}C	25.3437	0.3511	9.58363572	0,0038	0.3784	0.9957	0.1424

Table 4.3: Summary of d-spacing, crystallite size, strain, and lattice parameters of TiO_2-CeO_2 at different synthesis temperatures

Sample	**2θ(°)**	**d_{111}(nm)**	**D_{111}(nm)**	**Strain**	**a (nm)**	**V $(nm)^3$**
80°C	28,46275	0,313336	5,49010991	0,006594	0.5448358	0.16173
120°C	28,46273	0,313336	5,490215304	0,006594	0.5435374	0.16058
200°C	28,48007	0.313336	7,222465058	0,004799	0.5443392	0.16129
300°C	28,47914	0.313336	7,555432158	0,004792	0.5417046	0.15896

The morphology of the as-prepared pure CeO_2, TiO_2, and mixed metal oxides CeO_2 - TiO_2 was examined utilizing the SEM, as seen in **Fig. 4.2.** All the materials show nanoparticles, agglomerated. However, when increasing the synthesis temperature, the texture appears to be harder compared to those of lower synthesis temperature.

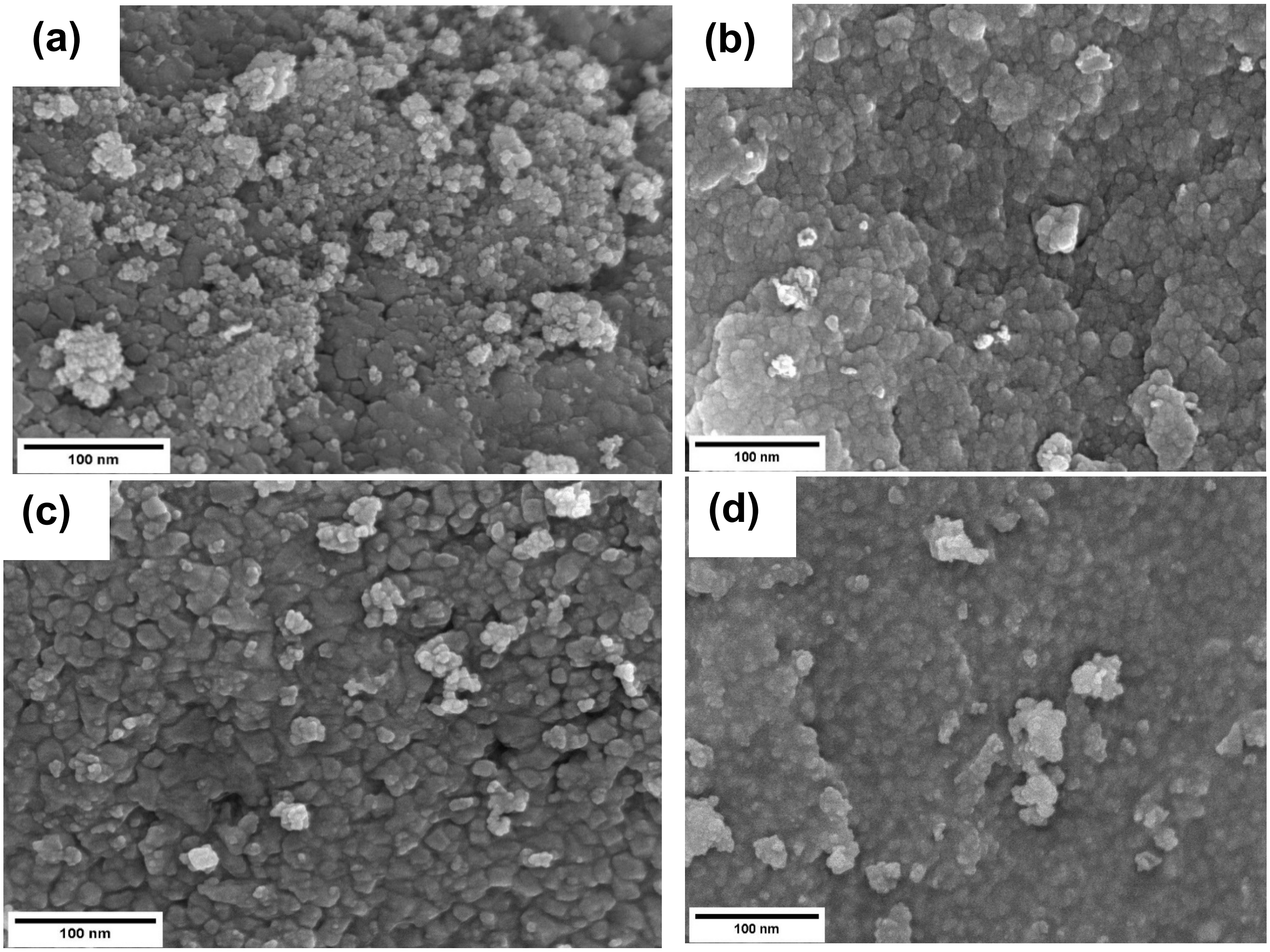

Fig. 4.2. SEM images of Mixed metal oxides at different temperatures, (a) 80°C; (b) 120°C; (c) 200°C and (d) 300°C

To study the influence of the synthesis temperature on the optical properties of the pure CeO_2, TiO_2, and mixed oxides nanostructures, UV–vis analyses were done as shown in **Fig. 4.3(a-c)**. As revealed in **Fig.4.3(a-c)**, the absorption spectra decrease when increasing the synthesis temperature for both pure materials and mixed oxides. This behavior is more visible for the materials synthesized at higher temperatures, i.e., 300 °C. Besides, the pure TiO_2, and mixed CeO_2-TiO_2, more reduction in the absorbance is noted.

The band gap energies were determined using Kubelka–Munk function:

(3)

Here (R) is the absolute value of reflectance and, F(R) is comparable to the absorption coefficient. The direct band gaps of CeO_2, TiO_2, and CeO_2-TiO_2 were estimated by plotting $[F(R)\cdot hv]^2$ vs. hv (eV). The attained bandgap energy (E_g) values are shown in Fig. 4(d-f). Clearly increasing the synthesis temperature, result in a reduction in the optical bandgap. Moreover, when preparing the mixed CeO_2-TiO_2 heterostructure, more reduction in the optical bandgap is observed, when the synthesis temperature increases to 300 °C. The reduced band gaps can be associated with the increase in grain size at higher annealing temperatures.

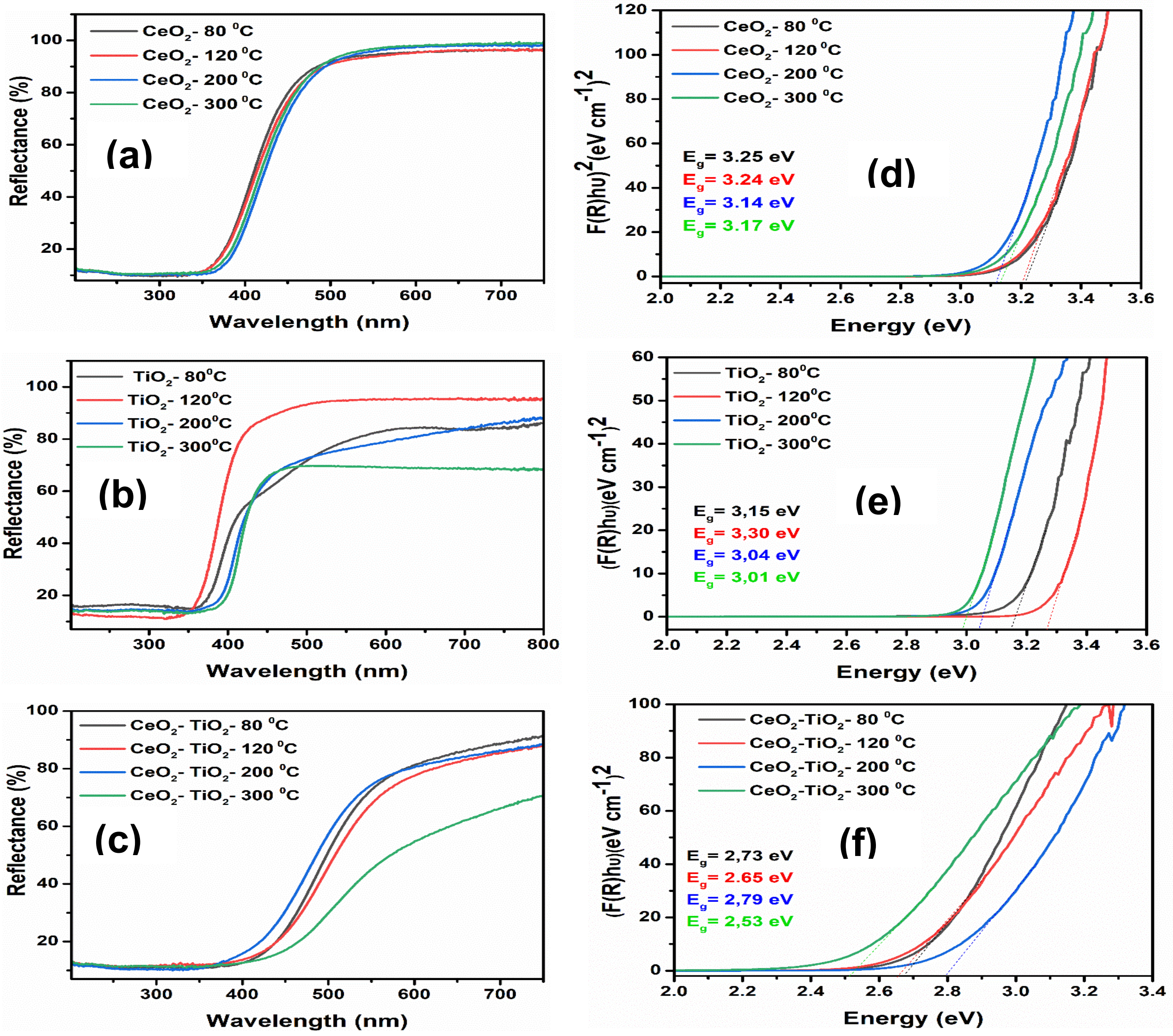

Fig.4. 4: UV-vis spectra of (a-c) pure CeO_2, $TiO_2$and CeO_2-TiO_2 heterostructure, and Tauc plot s of (d-f) pure CeO_2, Ti O_2, and CeO_2-TiO_2 heterostructure**.**

4.4. Conclusion

The pure CeO_2, TiO_2, and TiO_2-CeO_2 heterostructures were efficiently prepared using a sol-gel method. The structural studies demonstrated the formation of pure CeO_2, TiO_2, and TiO_2-CeO_2 heterostructure. SEM analyses exhibited that nanostructures are made of nanoparticles. Furthermore, the UV-vis analyses showed that the bandgaps of the pure CeO_2, TiO_2, and TiO_2-CeO_2 heterostructures reduce when increasing the synthesis temperature for all the nanostructures.

4.5 References

[4.1] Lian, X., Li, Y., Zhu, J., Zou, Y., An, D. and Wang, Q., 2019. Fabrication of Au-decorated SnO2 nanoparticles with enhanced n-buthanol gas sensing properties. Materials Science in Semiconductor Processing, 101, pp.198-205.

[4.2] Kim, T.H., Kwak, C.H. and Lee, J.H., 2017. NiO/NiWO4 Composite Yolk–Shell Spheres with Nanoscale NiO Outer Layer for Ultrasensitive and Selective Detection of Subppm-level p-Xylene. ACS applied materials & interfaces, 9(37), pp.32034-32043.

[4.3] Seo, M.H., Yuasa, M., Kida, T., Huh, J.S., Yamazoe, N. and Shimanoe, K., 2011. Microstructure control of TiO2 nanotubular films for improved VOC sensing. *Sensors and Actuators B: Chemical*, *154*(2), pp.251-256.

[4.4] Manibalan, G., Murugadoss, G., Thangamuthu, R., Kumar, R.M. and Jayavel, R., 2019. Facile synthesis of heterostructure CeO2-TiO2 nanocomposites for enhanced electrochemical sensor and solar cell applications. Journal of Alloys and Compounds, 773, pp.449-461.

[4.5] Ceria, P., 2017. CeO2-TiO2 for photoreduction of Co2 to methanol under visible light: effect of ceria loading. Malaysian Journal of Analytical Sciences, 21(1), pp.166-172.

[4.6] Yang, Y., Liang, Y., Wang, G., Liu, L., Yuan, C., Yu, T., Li, Q., Zeng, F. and Gu, G., 2015. Enhanced gas-sensing properties of the hierarchical TiO2 hollow microspheres with exposed high-energy {001} crystal facets. ACS applied materials & interfaces, 7(44), pp.24902-24908.

[4.7] Nisar, J., Topalian, Z., De Sarkar, A., Österlund, L. and Ahuja, R., 2013. TiO2-based gas sensor: a possible application to SO2. *ACS applied materials & interfaces*, *5*(17), pp.8516-8522.

[4.8] R. S. Jagath, F. K. Chong and D. W. Cecilia, "CeO2-TiO2 Photocatalyst: Ionic Liquid-Mediated Synthesis, Characterization, and Performance for Diisopropanolamine Visible Light Degradation," Bulletin of Chemical Reaction Engineering & Catalysis, vol. 13, no. 1, pp. 170-178, 2018.

[4.9] Ahmad, T., Shahazad, M., Ubaidullah, M. and Ahmed, J., 2018. Synthesis, characterization and dielectric properties of $$\hbox {TiO} _ {2} $$–$$\hbox {CeO} _ {2} $$ CeO2 ceramic nanocomposites at low titania concentration. Bulletin of Materials Science, 41(4), p.99.

[4.10] Ahmad, T., Shahazad, M., Ubaidullah, M. and Ahmed,J., 2018. Synthesis, characterization and dielectric properties of $$\hbox {TiO} _ CeO} _ CeO2 ceramic nanocomposites at low titania concentration. Bulletin of Materials Science, 41(4), p.99.

[4.11] Manibalan, G., Murugadoss, G., Thangamuthu, R., Kumar, R.M. and Jayavel, R., 2019. Facile synthesis of heterostructure CeO2-TiO2 nanocomposites for enhanced electrochemical sensor and solar cell applications. Journal of Alloys and Compounds, 773, pp.449-461.

[4.12] Fiorenza, R., Bellardita, M., D'Urso, L., Compagnini, G., Palmisano, L. and Scirè, S., 2016. Au/TiO2-CeO2 catalysts for photocatalytic water splitting and VOCs oxidation reactions. Catalysts, 6(8), p.121.

[4.13] Mohajan, H., 2011. Dangerous effects of methane gas in atmosphere.

[4.14] Choi, Y.J., Seeley, Z., Bandyopadhyay, A., Bose, S. and Akbar, S.A., 2007. Aluminum-doped TiO2 nano-powders for gas sensors. *Sensors and Actuators B: Chemical*, *124*(1), pp.111-117.

[4.15] G., Murugadoss, G., Thangamuthu, R., Kumar, R.M. and Jayavel, R., 2019. Facile synthesis of heterostructure CeO2-TiO2 nanocomposites for enhanced electrochemical sensor and solar cell applications. Journal of Alloys and Compounds, 773, pp.449-461.

[4.16] Oosthuizen, D.N., Motaung, D.E. and Swart, H.C., 2020. Gas sensors based on CeO2 nanoparticles prepared by chemical precipitation method and their temperature-dependent selectivity towards H2S and NO2 gases. Applied Surface Science, 505, p.144356.

[4.17] David E Motaung, Zamaswazi P Tshabalala, Peter R Makgwane, Fawzy A Mahmoud, Dina N Oosthuizen, Franscious R Cummings, Nompumelelo Leshabane, Nomso Hintsho-Mbita, Xiaogan Li, Suprakas S Ray, Hendrik C Swart, Multi-functioning of CeO2-SnO_2 heterostructure as room temperature ferromagnetism and chemiresistive sensors, Journal of Alloys and Compounds, 906 (2022) 164317.

[4.18] David E Motaung, Gugu H Mhlongo, Peter R Makgwane, Baban P Dhonge, Franscious R Cummings, Hendrik C Swart, Suprakas Sinha Ray, Ultra-high sensitive and selective H2 gas sensor manifested by interface of n–n heterostructure of CeO2-SnO2 nanoparticles, Sensors and Actuators B: Chemical 254 (2018) 984-995.

CHAPTER 5

$Cr_2O_3/TiO_2/CeO_2$ ternary heterojunction-based sensor for improved CH_4 performance

5.1. Introduction

The advancement of industry and the hastening of urbanization have led to serious problems associated with air pollution, where air pollutants concentrations have increased significantly. This has strongly affected the environment and human normal life. Moreover, the advancement in environmental awareness and the obligation for indoor air quality monitors have increased substantially. Among the flammable gases, methane (CH_4) is one of the most dangerous gases, it forms an explosive mixture once it is mixed with air. It has a tendency of exploding once it is exposed to heat and open flames. Furthermore it is amongst the record serious greenhouse gases because of its potential of greenhouse warming **[5.1-5.2]**. Therefore, it is necessary to develop a reliable and sensitive CH_4 sensor.is the simplest hydrocarbon. It is not only a major component of natural gas, but also an important raw material for syngas and many pharmaceutical chemicals. Therefore, the development of highly sensitive, selective, and low-cost sensors is in demand. At present, semiconductor metal oxides (SMOs)-based sensors have attracted significant attention due to their easy fabrication, affordability and suprior sensitivity to various toxic analytes **[5.3-5.5]**. So far studies have focused on using different approaches, such as the preparation of individual SMO materials, the introduction of elemental doping **[5.6]**, formation of heterostructures using mixed SMOs **[5.7-5.8]**, and the fabrication of metal-organic frameworks derived SMOs **[5.9-5.10]**. In contrast, the light activation of SMOs has shown to be much more effective to enhance the sensitivity of the gas sensors at room temperature **[5.11-5.13]**. Nevertheless, the higher UV light photon energy could lead to severe damage to eyes or human skin and this can strictly confine the sensor to be used in real-life applications **[5.14].** Moreover, SMOs functionalized with metal catalysts (Au, Pd, or Pt) have been used to improve the oxidative activity of CH_4 at minimal operational temperatures **[5.15-5.1519]**. To be specific, so far most of the studies have managed to operate their sensors for selected detection of CH_4 at operational temperatures ranging from 50 to 150 °C **[5.15-5.19]**. Thus, sensors that can operate at low temperatures, and still be able to produce high sensitivity and rapid response/recovery times are required.

Therefore, in the current work, we report on the low operational gas sensing for selective detection of CH_4 at high concentrations ranging from 1500 to 30 000 ppm. We show that by loading p-type Cr_2O_3 on the surface of the prepared n-n CeO_2/TiO_2 and TiO_2/CeO_2 structures, the p-n-n $Cr_2O_3/TiO_2/CeO_2$ ternary heterostructure resulted to superior response towards CH_4 at 100 °C. The higher response was justified by improved surface defects observed from the PL studies.

5.2. Experimental Details

5.2.1. Materials

All the reagents were used without any further purification. Titanium (IV) isopropoxide (Sigma-Aldrich), Cerium (III) Nitrate Hexahydrate, (Sigma-Aldrich), Chloroplatinic acid (Sigma-Aldrich), Polyvinylpyrrolidone (Sigma-Aldrich), Hexamethylenetetramine (Sigma-Aldrich), ethanol (Merck), NaOH (Merck) and distilled water.

5.2.2. Preparation of n/n-type TiO_2/CeO_2 and CeO_2/TiO_2 heterostructures

TiO_2/CeO_2 nanoparticles were Synthesis using hydrothermal method. 2.3 g of Ce $(NO_3)_3$. $6H_2O$ was dissolved in 20 mL water and 20 ml ethanol. A 0.5M NaOH stock solution was added dropwise into the solution and stirred with a magnetic stirrer for 6 hours. A 2mmol Ti $[OCH(CH_3)_2]_4$ and 2.5g PVP were added into the solution and stirred until a homogenous mixture was formed. The mixture was transferred into an autoclave Teflon vessel for 6 hours at 150 ºC. Then the precipitate was washed with ethanol and water, then dried in the oven at 80 ºC and calcined at 400 °C for 2 hours.

For the preparation of CeO_2/TiO_2 nanoparticles, a 2mmol Ti $[OCH(CH_3)_2]_4$ and 2.5g was dissolved in 20 mL water and 20 ml ethanol. A 0.5M NaOH solution was added dropwise into the solution and stirred with a magnetic stirrer for 6 hours. 2.3 g of Ce $(NO_3)_3$. $6H_2O$ and 2.5g PVP were added into the solution and stirred until a homogenous mixture was formed. The mixture was transferred into an autoclave Teflon vessel for 6 hours at 150 ºC. Then the precipitate was washed with ethanol and water, then dried in the oven at 80 ºC and calcined at 400 °C for 2 hours.

5.2.3. Preparation of p-n-n $Cr_2O_3/TiO_2/CeO_2$ ternary heterostructures

2.0 g Chromium (III) nitrate was loaded separately on TiO/CeO_2 and $CeO_2/$ TiO_2 nanoparticles under a magnetic stirrer. 2.4 g $C_6H_{12}N_4$ was added into the solution and stirred for 6hours. The mixture was then transferred into an autoclave Teflon vessel for 6 hours at 150 ºC. Then the precipitate was washed with ethanol and water, then dried in the oven at 80 ºC and calcined at 400 °C for 2 hours.

5.3. Characterization

The structure was investigated using the X-ray diffraction (XRD, Bruker AXS D8 Advance x-ray diffractometer, Cu Kα radiation λ= 0.154056). Scanning electron microscope (SEM, 3kV EHT, Zeiss) was used to probe the surface morphology. Room temperature photoluminescence (PL, spectrometer with a Kimmon IK series 325 nm laser) spectroscopy was utilized to probe the surface defects of the materials. UV-vis spectroscopy was used to probe the absorption spectra and optical bandgap of the materials.

5.4. Gas Sensors Fabrication and Analyses

The sensors performance was assessed using a commercial 4-channel Gas Mixing System (GMS) sensing equipment. Prior to measurements, few grams of TiO_2/CeO_2, CeO_2/TiO_2, $Cr_2O_3/TiO_2/CeO_2$ and $Cr_2O_3/CeO_2/TiO_2$ and Au loaded $Cr_2O_{43}/TiO_2/CeO_2$ nanostructured materials were mixed with ethanol and grinded in a mortar to form a paste, which was homogenously spread over the interdigital electrodes. The paste was dried for 10 hours at 80 °C to attain a proper adhesion. The fabricated-based sensors were placed in a Teflon chamber and tested for various gases, including benzene, ethylbenzene, toluene (BTE), ethanol, carbon monoxide, methane (CH_4), carbon dioxide (CO_2), and nitrogen dioxide (NO_2). The measurements were carried out at various operational temperatures (25, 50., 75, 100, 150, and 200 °C). The sensors were initially exposed to dry air for 3 h to sustain the resistance during the measurements. Thereafter, the sensors were exposed to the analyte gases for 20 min, and dry air was introduced for 40 min for proper recovery. The sensors were tested in dry air and relative humidity conditions. The sensing response was specified as R_a/R_g and R_g/R_a, for the reducing and oxidizing gas, respectively, denoting the resistance ratio of the sensor exposed to air (R_a) and the tested gases (R_g).

5.6 Results and Discussion

5.6.1. Structural Analysis

Fig. 5.1 depicts the XRD patterns of the n-n CeO_2/TiO_2, TiO_2/CeO_2, and p-n-n $Cr_2O_3/CeO_2/TiO_2$ and $Cr_2O_3/TiO_2/CeO_2$ heterostructures metal oxides. The peaks at 28.738°, 33.255°, 47.803°, and 56.745° correspond to typical CeO_2 fluorite structure reflections (JCPDS 34-0394). While the peak positions of the TiO_2 match well with JCPDS file number; 38-1479. An extra peak linked to the TiO_2 anatase phase was discovered by XRD at 25.34° (JCPDS No: 21-1272). This meant that Ti^{4+} ions injected into the CeO_2 lattice created a substitutional solid solution, which is advantageous for improved sensing properties. For Cr_2O_3 various peak positions are at 24.55°, 33.58°,36.20°, 50.17°, 54.84°, 63.38°, 65.10° and 72.99° which are indexed to the plane (012), (104), (110), (024), and (214), respectively. These peak positions match well with the JCPDS card No. 038–1479. The crystallite sizes were estimated using the Scherrer formula and the lattice parameters as listed in **Table 1.** The expansion of crystallite size is influenced by loading chromium oxide Cr_2O_3 on the surface of CeO_2/TiO_2 with the decreasing broadening of the diffraction (β) and decrease in strain, as seen in **Table 5.1** and **Fig. 1 (b)**. From **Fig. 1**, we noticed that Cerium dominates in CeO_2/TiO_2 mixed metal oxides, and the highest peak observed is from CeO_2, which means that the crystal size of the mixed metal oxide is determined by (111) peak, from CeO_2.

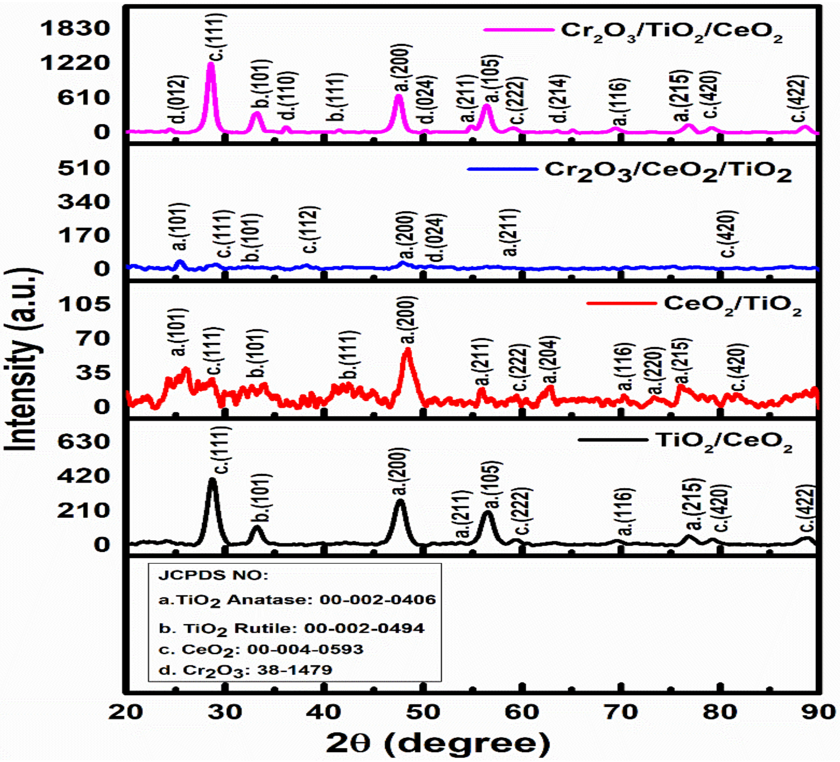

Fig. 5.1: XRD patterns of the CeO_2/TiO_2 p-type Cr_2O_3 on the surface of the prepared n-n CeO_2/TiO_2 and TiO_2/CeO_2 structures, the p-n-n $Cr_2O_3/TiO_2/CeO_2$.

Table 5.1: Summary of the d-spacing, crystallite sizes, and lattice parameters.

Sample	d_{111}(nm)	(β) FWHM (radians)	D_{111} (nm)	Strain	a (nm)	b (nm)	c (nm)	V $(nm)^3$
TiO_2/CeO_2	0.310634	0.0216	6.94	0,0020	0.3814	0,5414	0,38068	0,0786
CeO_2/TiO_2	0,313924	0.0288	5.18	0,0490	0.3756	0,5923	0,4114	0,0915
$Cr_2O_3/CeO_2/TiO_2$	0.311153	0.0367	4.07	0,0136	0.3782	0,5759	0,3969	0,0864
$Cr_2O_3/TiO_2/CeO_2$	0.312526	0.0144	10.40	0,0020	0.3825	0,5354	0,3810	0,0781

SEM micrographs of the TiO_2/CeO_2 in **Fig. 5.2 (a)** show spherical spheres made of nanoparticles, with a diameter in the range of 100 nm, and show a porous structure. While that in Fig. 5.2b shows agglomerated nanoparticles of CeO_2/TiO_2. By loading Cr_2O_3 on the surface as $Cr_2O_3/TiO_2/CeO_2$, nanoparticles that are entangled with one another as almost chain and very porous are observed. The diameter of these nanoparticles is roughly 50 nm. Nonetheless, for the structure of $Cr_2O_3/CeO_2/TiO_2$ in **Fig, 5.2 (d)**, short nanorods are observed.

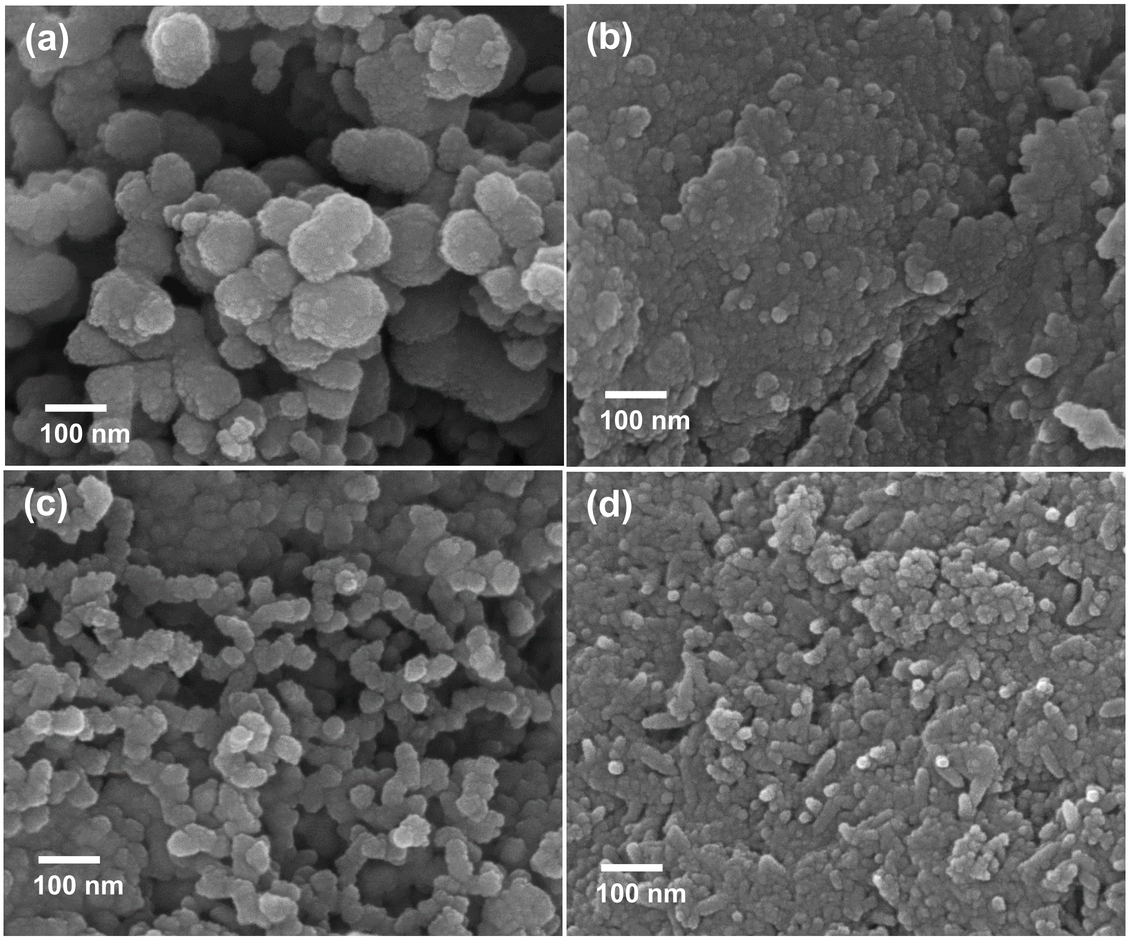

Fig. 5.2: (a) TiO_2/CeO_2, (b) CeO_2/TiO_2, (c) $Cr_2O_3/TiO_2/CeO_2$, and (d) $Cr_2O_3/CeO_2/TiO_2$

Fig. 5.3 shows the EDS elemental mapping of the $Cr_2O_3/TiO_2/CeO_2$ nanostructure. Clealry the TiO_2 and Cr_2O_3 are homogeneously distributed on the surface of CeO_2. Additionally, the only elements observed were Ce, Ti, Cr and O, without any impurities.

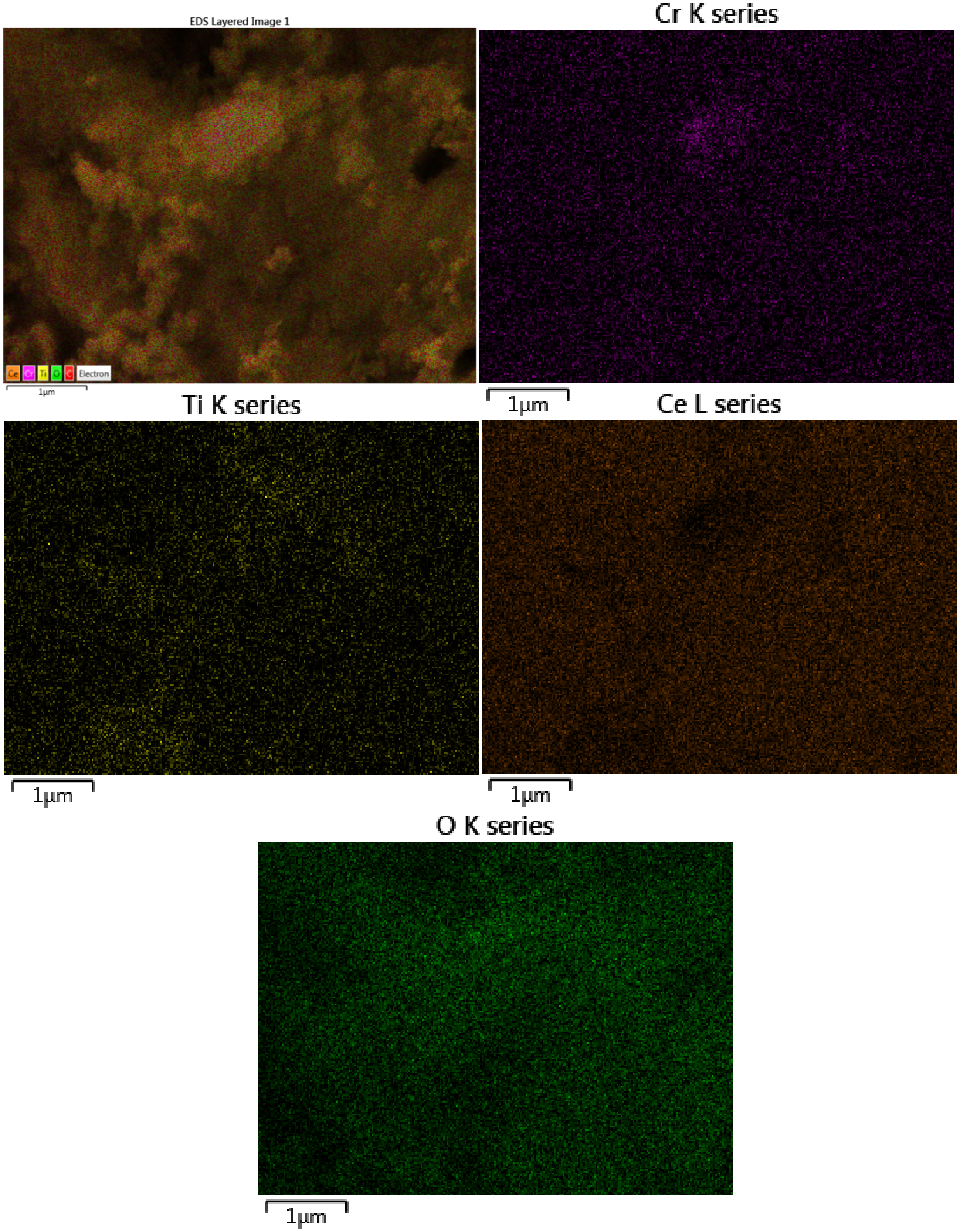

Fig. 5.3. EDS elemental mapping of the $Cr_2O_3/TiO_2/CeO_2$ nanostructure.

The UV–vis diffuse reflectance spectra in **Fig. 5.4(a)** show the influence of Cr_2O_3 loaded on the surface of TiO_2/CeO_2, and CeO_2/TiO_2. It indicates that the loading of Cr_2O_3 result in a reduction in the reflectance %. To determine the band gap energies, the Kubelka–Munk function was used as shown in Equ. 1:

(1)

where (R) is the absolute value of reflectance and F(R) is being equivalent to the absorption coefficient. The direct band gaps of TiO_2/CeO_2, CeO_2/TiO_2, $Cr_2O_3/CeO_2/TiO_2$, and $Cr_2O_3/TiO_2/CeO_2$ nanoparticles were estimated by plotting $[F(R)\cdot hv]^2$ vs. hv (eV). The linear part of the Tauc plot in **Fig. 5.4(b)** was extrapolated to $[F(R)\cdot hv]^2 = 0$ to get the direct band gap energy.

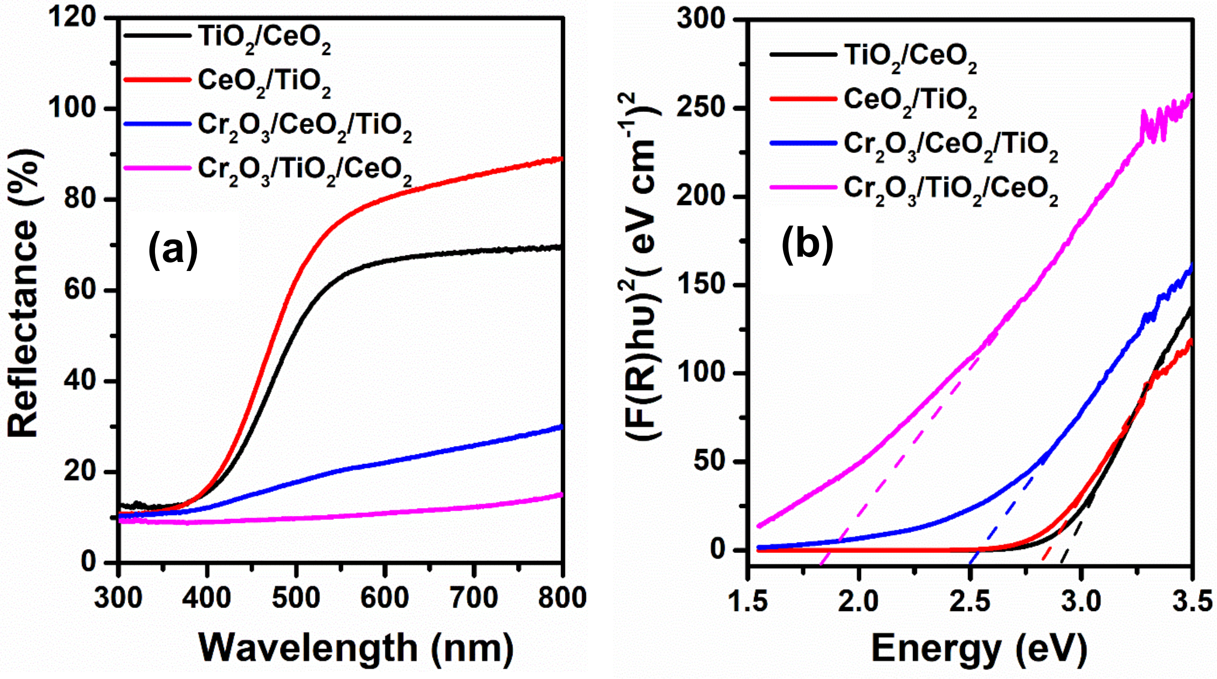

Fig. 5.4: (a) Diffuse reflectance spectra and (b) optical band gap estimated using the Kubelka–Munk function.

The obtained bandgap energy (E_g) values were 2.91, 2.83, 2.54, and 1.83, for TiO_2/CeO_2, CeO_2/TiO_2, $Cr_2O_3/CeO_2/TiO_2$, $Cr_2O_3/TiO_2/CeO_2$ nanoparticles, respectively. Indeed, the introduction of Cr_2O_3 on the surface of TiO_2/CeO_2, and CeO_2/TiO_2 has resulted to low optical band gaps, which could be beneficial in gas sensing.

To investigate the surface defects, PL studies were performed as shown in **Fig. 5.5**. As depicted in **Fig. 5.5a**, upon loading Cr_2O_3 on the surface of TiO_2/CeO_2, and CeO_2/TiO_2, the emission intensity increased, denoting that Cr_2O_3 induces surface defects, more especially on $Cr_2O_3/TiO_2/CeO_2$ structure. By deconvoluting the peaks using Gaussian Fit, the TiO_2/CeO_2 shows peaks located at 2.42, 2.60, and 2.92 eV. While the CeO_2/TiO_2 peaks are positioned at 2.32, 2.80, and 3.16 eV. The peak at 2.3-2.4 is associated with deep oxygen vacancy-related trap states (i.e., Ti^{3+} and F^+ centres) **[5.21-5.23]**. While the peaks at 2.60 and 2.80 eV are associated with the oxygen vacancies (V_O) in Ce-4f and O-2p states **[5.24]**. The peak at 2.91 eV is linked to self-trapped excitons at TiO_6 octahedral **[5.25]**. By loading Cr_2O_3 peaks at 2.41, 2.80, 3.01, and 3.26 eV for Cr_2O_3/ CeO_2/TiO_2 and 2.22, 2.70, 3.00, and 3.27 eV for $Cr_2O_3/CeO_2/TiO_2$, respectively. The emissions at 3.01-3.26, and 2,2 eV can be ascribed to near band edge (NBE), and e involvement of mid-gap trap states, such as surface defects and V_O in Cr_2O_3, respectively **[5.26-5.28]**

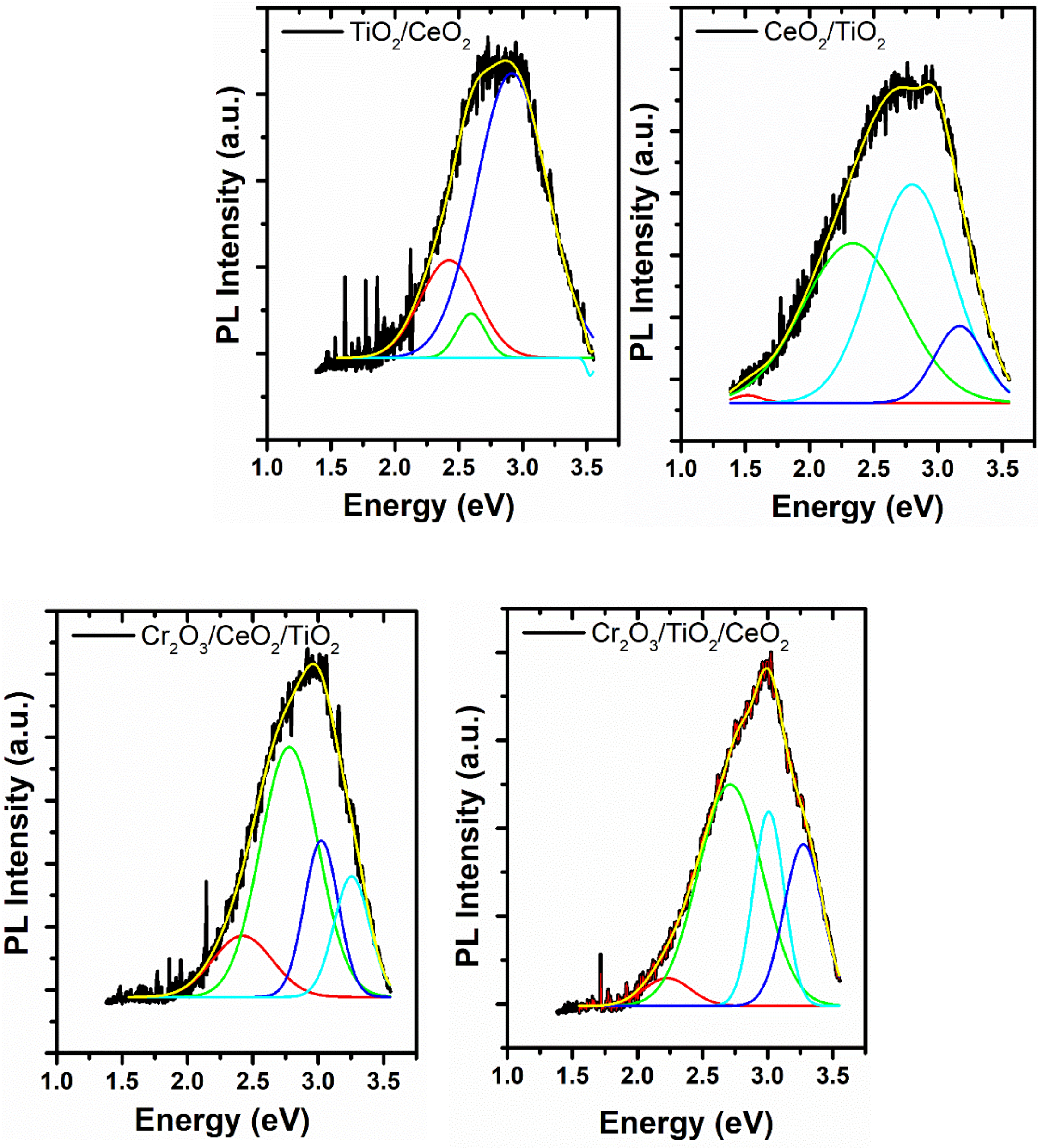

Fig.5. 5: (a) PL spectra of CeO_2/TiO_2, TiO_2/CeO_2, $Cr_2O_3/CeO_2/TiO_2$, and $Cr_2O_3/TiO_2/CeO_2$.

5.6.2 Gas Sensing Analyses

CeO_2 and TiO_2 are known as n-type materials, while the Cr_2O_3 is considered a p-type semiconductors. When compared to sensing components of n/n type conductivity of CeO_2/TiO_2 and TiO_2/CeO_2, the p/n/n type conductivity of $Cr_2O_3/TiO_2/CeO_2$ and $Cr_2O_3/CeO_2/TiO_2$ heterostructure can be very attractive based on the intrinsic advantage induced by the combination of the surface nanostructure and improved surface area, which could lead to superior sensing capability. Thus, since the operational temperature has a significant effect on the SMOs-based gas sensors' performance, therefore the change in resistance in air (i.e., R_a) values of CeO_2/TiO_2, TiO_2/CeO_2, $Cr_2O_3/TiO_2/CeO_2$, and $Cr_2O_3/CeO_2/TiO_2$ heterostructure-based sensors is investigated. As shown in Fig. 5a, the sensors R_a decrease with operational temperature. his behavior could be associated with thermal excitation, since the valence band of the p-type SMO possesses more hole carriers, as the operational temperature increases. Thus, this leads to a reduction in the R_a values of the sensors. This typical behavior is in-line with the conduction features of semiconductor nanostructured materials **[5.29-5.30]**. Fig. 5b and c shows the real-time resistance of the sensors tested towards various concentrations of CH_4 at various operational temperatures (i.e., 100 and 200 °C). No resistance change is observed for the CeO_2/TiO_2 and TiO_2/CeO_2, $Cr_2O_3/CeO_2/TiO_2$-based sensors at 100 °C. Nonetheless, for the $Cr_2O_3/TiO_2/CeO_2$-based sensor, a change in resistance is observed at 100 °C.

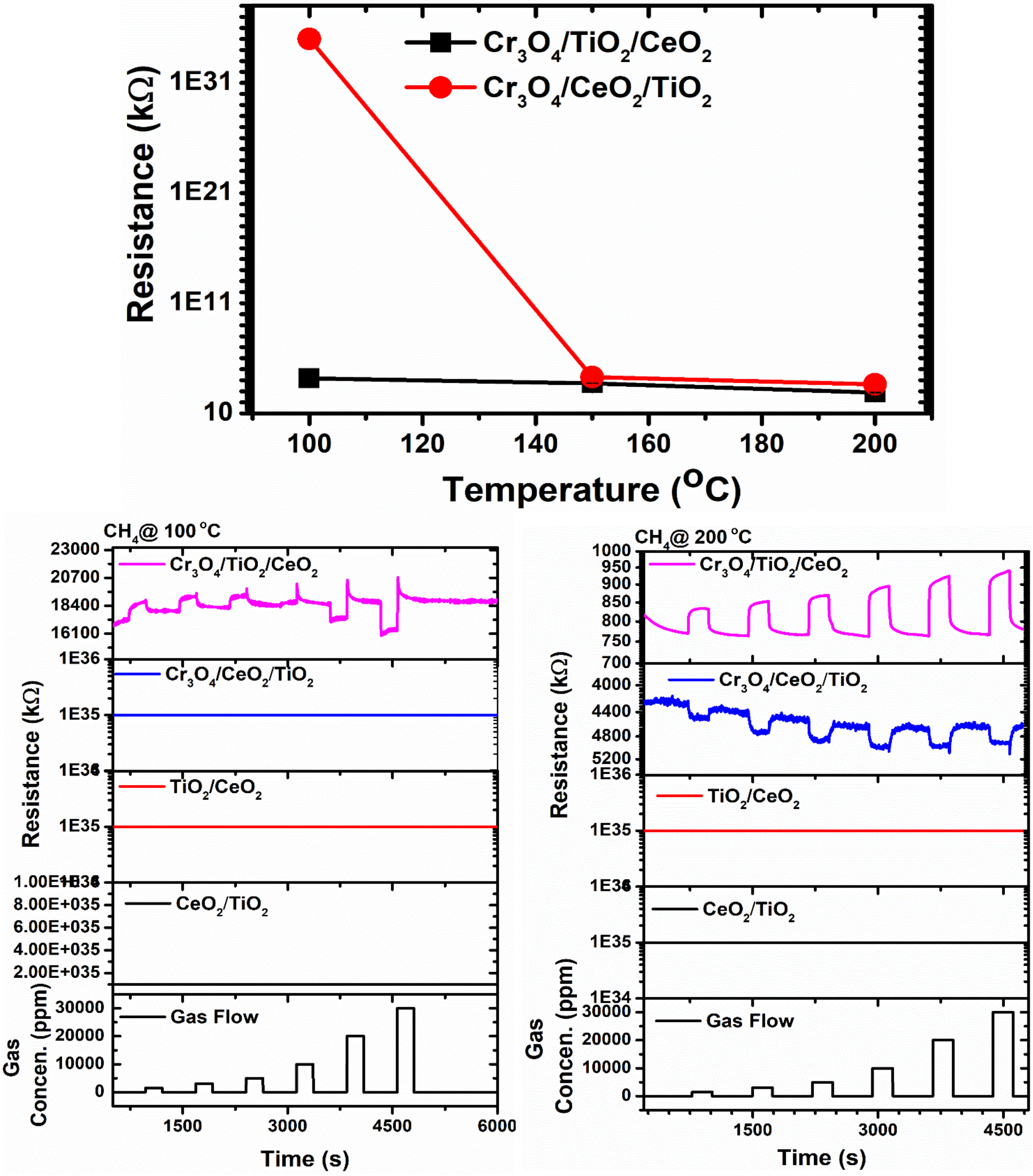

Fig. 5.6. (a) The Ra values of three sensors and (b) their responses towards 50 ppm CH_4 at different operating temperatures.

Fig. 5.7a shows that at 100 °C operational temperature, a $Cr_2O_3/TiO_2/CeO_2$-based sensor shows a p-type conductivity at low CH_4 concentration (1500-10 000 ppm). Interestingly, at higher concentrations (20 000 - 30 000 ppm), the sensor resistance switches to an n-type conductivity. This behavior was reported on previous studies. Furthermore, when increasing the operational temperature (i.e., at 150 to 200 °C), the sensor shows a p-type conductivity, though at this time no switching is observed even at higher gas concentrations.

The response versus the operational temperature is depicted in Fig. 5.7b. A superior response of 1.53 is observed at 100 °C, for the $Cr_2O_3/TiO_2/CeO_2$-based sensor. When increasing the temperature, the response of both sensors reduces denoting that the optimized temperature is 100 °C. The higher response of the $Cr_2O_3/TiO_2/CeO_2$-based sensor, compared to other sensors could be associated with higher V_O observed in PL analyses. Moreover, the smaller bandgap observed for the $Cr_2O_3/TiO_2/CeO_2$-based sensor denotes that the electrons may be more inclined to change and result in more photogenerated carriers that could lead to enhanced sensing response and therefore lead to reduced sensing temperature.

Fig. 5.7c discloses the relationship between the responses of the sensor and the CH_4 concentrations (1500-30 000 ppm) at 100 °C. An increase in the response, which shows exponential growth with the CH_4 concentration is observed. Fig. 5.7d shows the sensitivity of the $Cr_2O_3/TiO_2/CeO_2$-based sensor.

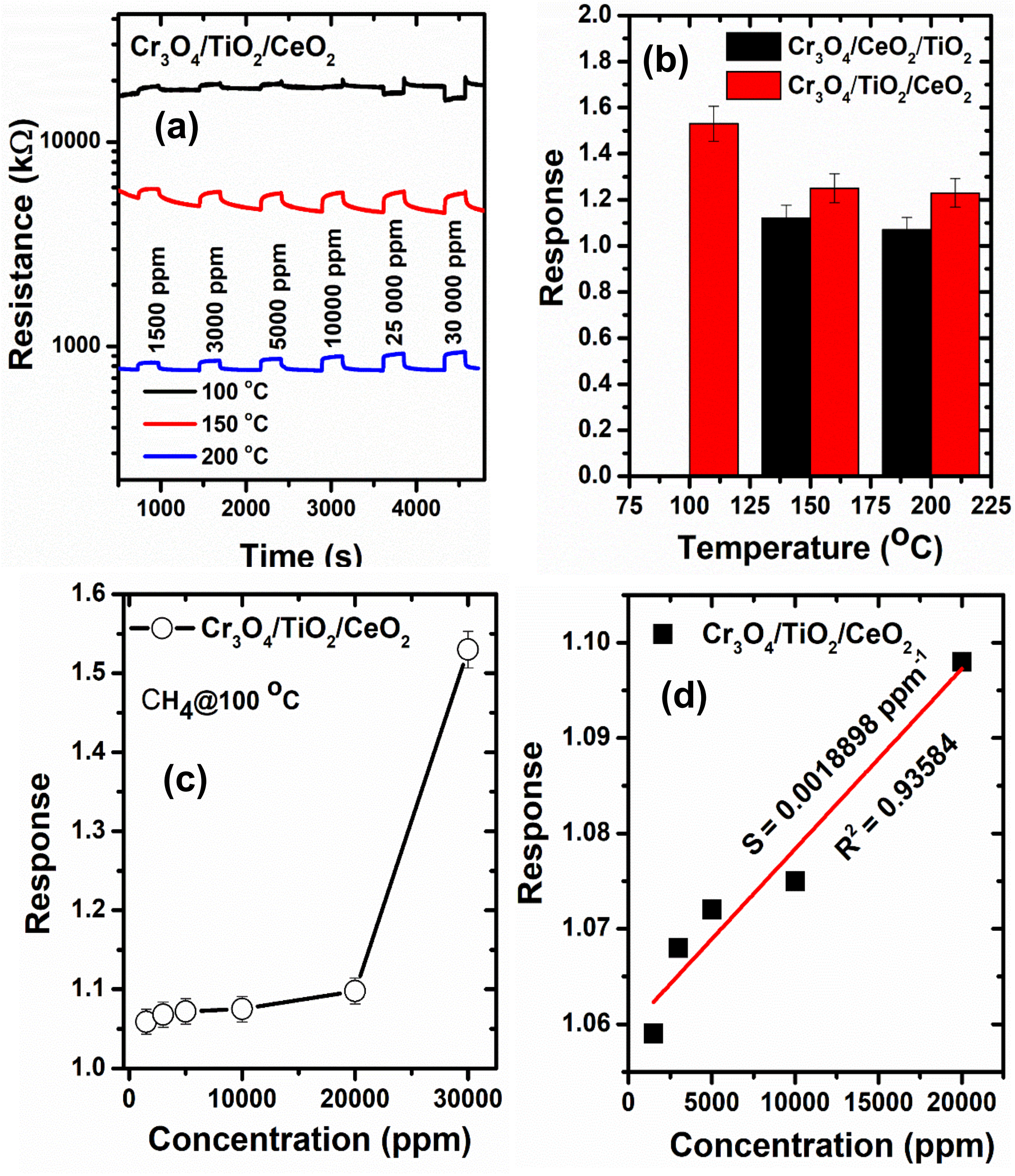

Fig. 5.7: Real-time resistance plot at various temperatures, (b) response versus temperature, and (c) response versus concentration, and (d) sensitivity plot of $Cr_2O_3/TiO_2/CeO_2$-based sensor.

Selectivity is also one of the most vital parameters for gas sensing in real-time practical applications. **Fig. 5.8** depicts the radar plots showing the selectivity and cross-selectivity of various sensors towards 30 000 ppm CH_4 in the presence of other interference gases, such as CO (100 ppm), ethanol (125 ppm), NO_2 (400 ppm) and CO_2 (1500 ppm), tested at 100 °C. Studies have shown that a higher concentration of CH_4 of about 4–5 % (i.e., 40 000-50 000 ppm) in the air could result in an explosion **[5.31]**. On the other hand, is the National Institute for Occupational Safety and Health (NIOSH) has set an exposure of 1000 ppm as Threshold Limit Value (TLV) for 8-hours **[5.32]**. Thus, in the radar plot in **Fig. 5.8a**, the p-n-n $Cr_2O_3/TiO_2/CeO_2$ ternary heterostructure shows an excellent response towards CH_4, while other sensors disclosed a weak response. Besides, the sensor also showed a lower response towards ethanol vapor.

To validate this finding, we calculate the cross-selectivity using the following expression: $K = S_{benzene}/S_0$ **[5.33]**, where K is the selectivity coefficient and S_{CH4} is linked $Cr_2O_3/TiO_2/CeO_2$ ternary heterostructure-based sensor response and S_0 is associated to the response of the interfering gases (i.e., CO, ethanol, CO_2, and NO_2). **Fig. 6b** shows cross-sensitivity values for benzene and xylene, respectively. The higher 'K' value denotes the superior selectivity of the $Cr_2O_3/TiO_2/CeO_2$ ternary heterostructure towards CH_4 at 100 °C.

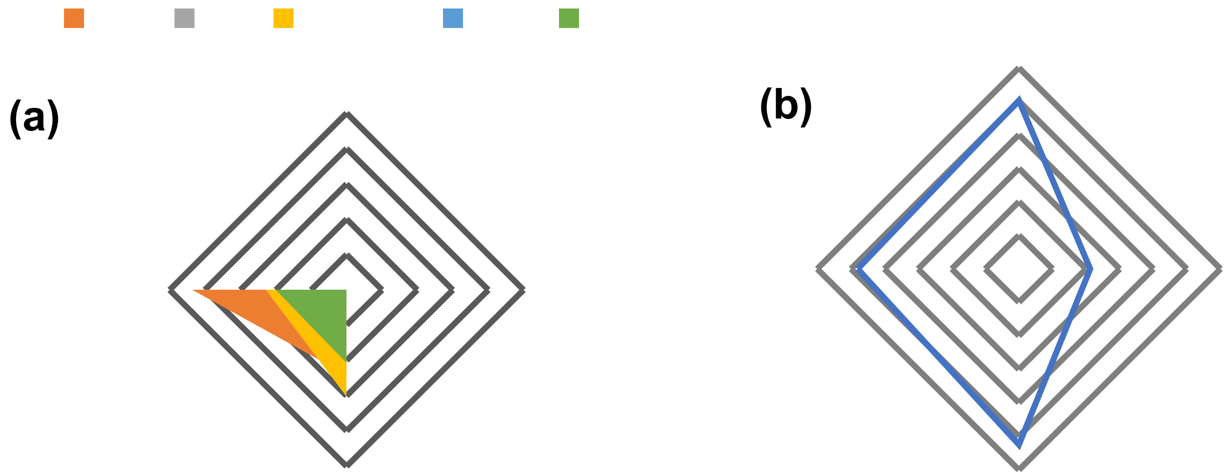

Fig. 5.8: **(a)** Radar selectivity and (b) radar cross-sensitivity plots of the p-n-n $Cr_2O_3/TiO_2/CeO_2$ and $Cr_2O_3/CeO_2/TiO_2$.

Additionally, the CH_4 sensing results of our current work compared with the other sensors are listed in **Table 5.2**. As shown in **Table 5.2**, our sensor indeed shows a higher response in comparison to those in the literature. Besides, some of the sensors operational temperature is very high compared to our current sensor.

Table 5.2 Comparison of CH_4-sensing performance of various sensors

Sensing element	Conc. (ppm)	Response	Temp. (°C)	Refs.
$Cr_2O_3/TiO_2/CeO_2$	30 000	3.9 %	100	**This work**
ZnO film/Pd-Ag	10,000	82 %	100	**[5.34]**
ZnO/rGO composites	1500	14 %	190	**[5.35]**
SnO_2 nanorods/ graphene	1000	24.9 %	150	**[5.36]**
MWCNT/Pd	20,000	7 %	R.T.	**[5.37]**
ZnO microwire	2000	5 %	R.T.	**[5.38]**
Au/VOx films	1000		R.T.	**[5.39]**
MgO/TiO_2	1000	1.77 %	300	**[5.40]**
NiO/In_2O_3	10,000	13.06 %	120	**[5.41]**
CuO/In_2O_3	10,000	2.85 %	100	**[5.42]**
Ag/ZnO	5000	20.15 %	200	**[5.43]**
Pt/SnO_2	1000	4.5 %	350	**[5.44]**
ZnO/NiO	1000	34.2 %	340	**[5.45]**

5.7 Conclusion and Remarks

The TiO_2/CeO_2, CeO_2/TiO_2, $Cr_2O_3/TiO_2/CeO_2$ and Cr_2O_3/CeO_2TiO_2-based sensors were successfully fabricated. Structural analyses validated the formation of ternary heterostructure. Among the tested sensors, the $Cr_2O_3/TiO_2/CeO_2$-based sensor displayed a remarkable response and selectivity towards CH_4 at low operational temperature of 100 °C. Additionally, a smaller response toward ethanol was also observed for the $Cr_2O_3/TiO_2/CeO_2$-based sensor.

The higher response observed for the $Cr_2O_3/TiO_2/CeO_2$-based sensor towards CH_4 was further validated by PL studies, which showed that the material consisted of higher V_O, which could be the reason for the improved sensing performance. Additionally, the UV-vis analyses also confirmed that the material has a smaller bandgap, which denoted that the electrons were more inclined to change and resulting in more photogenerated carriers that could lead to enhanced sensing response and therefore lead to reduced sensing temperature.

5.8 References

[5.1] J. Xia, F. Zhu, S. Zhang, A. Kolomenskii, H. Schuessler, A ppb level sensitive sensor for atmospheric methane detection, Infrared Phys Technol 86 (2017) 194–201.

[5.2] Z.P. Tshabalala, H.C. Swart, D.E. Motaung, Fabrication of TiO_2 nanofibers based sensors for enhanced CH4 performance induced by notable surface area and acid treatment, Vacuum 187 (2021) 110102.

[5.3] J. Tian, B. Jiang, H. Shao, Y. Wang, T. Wang, F. Li, D. Li , Y. Yang , X. Dong, A new strategy to one-step construct polyoxometalate/semiconductor one-dimensional tandem heterojunctions toward optimized conductometric sensing performances of ethanol gas, Sensors and Actuators: B. Chemical 374 (2023) 132797. https://doi.org/10.1016/j.snb.2022.132797.

[5.4] H. Wang et al. Gas sensing materials roadmap J. Phys.: Condens. Matter 33 (2021) 303001. DOI 10.1088/1361-648X/abf477.

[5.5] D.E Motaung, Z.P. Tshabalala, P.R. Makgwane, F.A. Mahmoud, D.N. Oosthuizen, F.R. Cummings, N. Leshabane, N. Hintsho-Mbita, X. Li, S.S. Ray, H.C. Swart, Multi-functioning of CeO_2-SnO_2 heterostructure as room temperature ferromagnetism and chemiresistive sensors, Journal of Alloys and Compounds, 906 (2022) 164317.

[5.6] Y. Wang, X. Sun, J. Cao, Enhanced methane sensing performance of Ag modified In_2O_3 microspheres, Journal of Alloys and Compounds 895 (2022) 162557.

[5.7] C. Han, X. Li, Jie Liu, Haipeng Dong, Wanying Cheng, Yu Liu, Jiayu Xin, Xinghua Li, Changlu Shao, Yichun Liu, In_2O_3/g-C_3N_4/Au ternary heterojunction-integrated surface plasmonic and charge-separated effects for room-temperature ultrasensitive NO_2 detection, Sensors and Actuators: B. Chemical 371 (2022) 132448.

[5.8] S. Gao, Y. Zhao, W. Wang, J. Zhao, X. Wang, Au/CuO/Cu_2O heterostructures for conductometric triethylamine gas sensing, Sensors and Actuators: B. Chemical 371 (2022) 132515

[5.9] C. Zhu, R.E.GeraldII, Y. Chen, J. Huang, Metal-organic framework portable chemical sensor, Sensors and Actuators B: Chemical, 321 (2020) 128608.

[5.10] S. Wu, X. Li, Y. Xu, J. Wu, Z. Wang, Y. Han, X. Zhang,Hierarchical spinel $Ni_xCo_{1-x}Fe_2O_4$ microcubes derived from Fe-based MOF for high-sensitive acetone sensor, Ceramics International, 44, (2018) 19390-19396.

[5.11] Z. Li, X. Pan, Z. Yi, Photocatalytic oxidation of methane over CuO-decorated ZnO nanocatalysts, J. Mater. Chem. A Mater. Energy Sustain. 7 (2019) 469–475.

[5.12] L. Meng, Z. Chen, Z. Ma, S. He, Y. Hou, H.H. Li, R. Yuan, X.H. Huang, X. Wang, X. Wang, J. Long, Gold plasmon-induced photocatalytic dehydrogenative coupling of methane to ethane on polar oxide surfaces, Energy Environ. Sci. 11 (2018) 294–298.

[5.13] R. Chen, J. Wang, S. Luo, L. Xiang, W. Li, D. Xie, Unraveling photoexcited electron transfer pathway of oxygen vacancy-enriched ZnO/Pd hybrid toward visible light-enhanced methane detection at a relatively low temperature, Appl. Catal. B Environ. 264 (2020) 118554.

[5.14] H. Wang, J. Bai, M. Dai, K. Liu, Y. Liu, L. Zhou, F. Liu, F. Liu, Y. Gao, X. Yan, L. Geyu, Visible light activated excellent NO_2 sensing based on 2D/2D ZnO/g-C3N4 heterojunction composites, Sens. Actuators B Chem. 304 (2020), 127287.

[5.15] D. Haridas, V. Gupta, Enhanced response characteristics of SnO_2 thin film-based sensors loaded with Pd clusters for methane detection, Sens. Actuators B Chem. 166 (2012) 156–164. [5.16] D. Zhang, H. Chang, Y. Sun, C. Jiang, Y. Yao, Y. Zhang, Fabrication of platinum-loaded cobalt oxide/molybdenum disulfide nanocomposite toward methane gas sensing at low temperature, Sens. Actuators B Chem. 252 (2017) 624–632.

[5.17] N.M. Vuong, D. Kim, H. Kim, Porous Au-embedded WO_3 nanowire structure for efficient detection of CH4 and H_2S, Sci. Rep. 5 (2015), 11040.

[5.18] R. Kumar, X. Liu, J. Zhang, M. Kumar, Room-temperature gas sensors under photoactivation: from metal oxides to 2D materials, Nano-Micro Lett. 12 (2020) 1–37.

[5.19] X. Chen, Y. Li, X. Pan, D. Cortie, X. Huang, Z. Yi, Photocatalytic oxidation of methane over silver decorated zinc oxide nanocatalysts, Nat. Commun. 2016 (2016), 12273.

[5.20] M.B. Kgomo a,b , K. Shingange a , M.I. Nemufulwi a,b , H.C. Swart b , G.H. Mhlongo, Belt-like In_2O_3 based sensor for methane detection: Influence of morphological, surface defects and textural behavior Materials Research Bulletin 158 (2023) 112076

[5.21] Z.P. Tshabalala, H.C. Swart, D.E. Motaung, Fabrication of TiO_2 nanofibers based sensors for enhanced CH_4 performance induced by notable surface area and acid treatment, Vacuum 187 (2021) 110102.

[5.22] B. Santara, P.K. Giri, K. Imakita, M. Fujii, Evidence of oxygen vacancy induced room temperature ferromagnetism in solvothermally synthesized undoped TiO2 nanoribbons, Nanoscale 5 (2013) 5476–5488.

[5.23] C. Mercado, Z. Seeley, A. Bandyopadhyay, S. Bose, J.L. McHale, Photoluminescence of dense nanocrystalline titanium dioxide thin films: effect of doping and thickness and relation to gas sensing, Appl. Mater. Interfaces 3 (2011) 2281–2288.

[5.24] D.N. Oosthuizen, DE Motaung, HC Swart, Gas sensors based on CeO_2 nanoparticles prepared by chemical precipitation method and their temperature-dependent selectivity towards H_2S and NO_2 gases, Applied Surface Science 505 (2020) 144356.

[5.25] Z.P. Tshabalala, K. Shingange, B.P. Dhonge, O.M. Ntwaeaborwa, G.H. Mhlongo, D.E. Motaung, Fabrication of ultra-high sensitive and selective CH_4 room temperature gas sensing of TiO_2 nanorods: Detailed study on the annealing temperature, Sensors and Actuators B: Chemical, 238 (2017) 402-419.

[5.26] J.H. Liang, Z.X. Deng, X. Jiang, F.L. Li, Y.D. Li, Photoluminescence of tetragonal ZrO_2 nanoparticles synthesized by microwave irradiation Inorg Chem, 41 (2002), pp. 3602-3604

[5.27] A. Boukhachem, O. Kamoun, C. Mrabet, C. Mannai, N. Zouaghi, A. Yumak, *et al.*

Structural, optical, vibrational and photoluminescence studies of Sn-doped MoO_3 sprayed thin films, Mater Res Bull, 72 (2015), pp. 252-263

[5.28] T. Larbi, M.A. Amara, B. Ouni, M. Amlouk, Enhanced photocatalytic degradation of methylene blue dye under UV-sunlight irradiation by cesium doped chromium oxide thin films, Mater Res Bull, 95 (2017), pp. 152-162.

[5.29] Zamaswazi P Tshabalala, Teboho P Mokoena, Mudalo Jozela, James Tshilongo, Thembela K Hillie, Hendrik C Swart, David E Motaung, TiO_2 Nanowires for Humidity-Stable Gas Sensors for Toluene and Xylene, ACS Applied Nano Materials, 4 (2021) 702-716.

[5.30] Rapelang G Motsoeneng, Ioannis Kortidis, Rirhandzu Rikhotso, Hendrik C Swart, Suprakas Sinha Ray, David E Motaung, Temperature-dependent response to C3H7OH and C2H5OH vapors induced by deposition of Au nanoparticles on SnO2/NiO hollow sphere-based conductometric sensors, Sensors and Actuators B: Chemical, 316 (2020) 128041.

[5.31] J. Liu, G. Li, A remote sensor for detecting methane based on palladium-decorated single walled carbon nanotubes, Sensors 13 (2013) 8814–8826.

[5.32] Hazardous Substance Fact Sheet https://nj.gov/health/eoh/rtkweb/documents/fs/1202.pdf (accessed on the 12th of December 2022).

[5.33] Y.-M. Jo, T.-H. Kim, C.-S. Lee, K. Lim, C.W. Na, F. Abdel-Hady, A.A. Wazzan, J.-H. Lee, Metal−organic framework-derived hollow hierarchical Co_3O_4 nanocages with tunable size and morphology: ultrasensitive and highly selective detection of methylbenzenes, ACS Appl. Mater. Interfaces, 10 (2018) 8860-8868.

[5.34] S. Ghosh, C.R. Chaudhuri, R. Bhattacharya, H. Saha, N. Mukherjee, Palladium silver-activated ZnO surface: highly selective methane sensor at reasonably low operating temperature, ACS Appl. Mater. Interfaces 6 (2014) 3879–3887.

[5.35] D. Zhang, N. Yin, B. Xia, Facile fabrication of ZnO nanocrystalline-modified graphene hybrid nanocomposite toward methane gas sensing application, J. Mater. Sci: Mater. Electron. 26 (2015) 5937–5945

[5.36] M. Kooti, S. Keshtkar, M. Askarieh, A. Rashidi, Progress toward a novel methane gas sensor based on SnO_2 nanorods-nanoporous graphene hybrid, Sens. Actuators B Chem. 281 (2019) 96–106.

[5.37] Y. Li, H. Wang, Y. Chen, M. Yang, A multi-walled carbon nanotube/palladium nanocomposite prepared by a facile method for the detection of methane at room temperature, Sens. Actuators B Chem. 132 (2008) 155–158.

[5.38] G.Y. Chai, O. Lupan, E.V. Rusu, G.I. Stratan, V.V. Ursaki, V. S¸ ontea, H. Khallaf, L. Chow, Functionalized individual ZnO microwire for natural gas detection, Sens. Actuators A Phys. 176 (2012) 64–71.

[5.39] J. Liang, J. Liu, N. Li, W. Li, Magnetron sputtered Au-decorated vanadium oxides composite thin films for methane-sensing properties at room temperature, J. Alloys Compds. 671 (2016) 283–290.

[5.40] B.C. Sertel, N.A. Sonmez, M.D. Kaya, S. Ozcelik, Development of MgO:TiO_2 thin films for gas sensor applications, Ceram. Int 45 (2019) 2917–2921.

[5.41] Y. Wang, M. Yao, R. Guan, Z. Zhang, J. Cao, Enhanced methane sensing performance of NiO decorated In_2O_3 nanospheres composites at low temperature, J. Alloy. Compd. 854 (2021) 157169.

[5.42] N.M. Shaalan, D. Hamad, O. Saber, Co-Evaporated CuO-Doped In_2O_3 1DNanostructure for Reversible CH_4 Detection at Low Temperatures: structural phase change and properties, Materials 12 (2019) 4073.

[5.43] Y. Wang, Y.Y. Cui, X.N. Meng, Z.Y. Zhang, J.L. Cao, A gas sensor based on Agmodified ZnO flower-like microspheres: temperature-modulated dual selectivity to CO and CH_4, Surface. Interfac. 24 (2021), 101110.

[5.44] W. Lu, D.G. Ding, Q.Z. Xue, Y.G. Du, Y. Xiong, J.Q. Zhang, X.L. Pan, W. Xing, Great enhancement of CH4 sensitivity of SnO_2 based nanofibers by heterogeneous sensitization and catalytic effect, Sens. Actuators, B 254 (2018) 393–401.

[5.45] S.S. Zhang, Y.W. Li, G. Sun, B. Zhang, Y. Wang, J.L. Cao, Z.Y. Zhang, Synthesis of NiO-decorated ZnO porous nanosheets with improved CH_4 sensing performance, Appl. Surf. Sci. 497 (2019.

CHAPTER 6

SUMMARY AND FUTURE WORKS

In summary CeO_2, TiO_2, and TiO_2-CeO_2 heterostructure were successfully prepared using a sol-gel method. The fabricated CeO_2, TiO_2, and TiO_2-CeO_2 heterostructure-based sensors showed no response towards various tested gases. Basically, the sensors displayed higher resistance, which overloaded at the temperature ranging from 25 to 250 °C. Such poor sensing performances were justified by adopted synthesis and approach used for the preparation of the nanomaterials. This assumption is justified by that upon loading TiO_2 on the CeO_2 surface and CeO_2 on the TiO_2 surface using hydrothermal approach, the fabricated sensors (TiO_2/CeO_2 and CeO_2/TiO_2) showed a response towards CH_4 at 200 °C. This behavior clearly shows that the synthesis method has an effect on the sensing characteristics.

Therefore, to improve the performance of the sensors towards CH_4, p-type Cr_2O_3 SMO was loaded on the surface of both TiO_2/CeO_2 and CeO_2/TiO_2 heterostructures. Among the fabricated sensors, the $Cr_2O_3/TiO_2/CeO_2$-based sensor exhibited an extraordinary sensitivity and selectivity towards CH_4 gas at 100 °C. Such superior performance was justified by improved surface defects, like V_O, which played a vital part as active sites for adsorption CH_4 molecules. Moreover, the reduced band compared to other materials was the reason for reduced operational temperature. Basically, reduced bandgap, denotes that the electrons will be more inclined to change and result in more photogenerated carriers that can result in enhanced sensing response and therefore lead to a reduced sensing temperature.

Future study will focus on studying the long-term stability of the materials in dry air and in the presence of relative humidity ranging from 10- 60 %. The repeatability analyses will also be carried out at different conditions. Besides, more interference gases, such as BTEX will be investigated. The loading of TiO_2/CeO_2 and CeO_2/TiO_2 heterostructures with various p-type materials, such as NiO, Mn_3O_4, Co_3O_4, etc. will also be carried out. Moreover, the loading or doping of noble metals will also be the focus of the future work.